On the Origin of the Photospheric Magnetic Field

Peter W. Schuck,[1] Mark G. Linton,[2] Kalman J. Knizhnik,[2] and James E. Leake[1]

[1] *Heliophysics Science Division, NASA Goddard Space Flight Center, 8800 Greenbelt Road, Greenbelt, MD 20771, USA*
[2] *Space Science Division, US Naval Research Laboratory, 4555 Overlook Avenue, SW, Washington, DC, USA*

(Received March 14, 2022; Revised May 17, 2022; Accepted May 24, 2022)

ABSTRACT

This article presents results that challenge the paradigms that (1) the convection zone is the source of the radial magnetic field in the photosphere and (2) that coronal currents are neutralized from the perspective of the photosphere. We demonstrate, using a new analysis tool applied to simulations and observations, that bare or partially dressed current channels are supported by the solar corona and that fingerprints of these coronal current systems can be detected in the photosphere. These coronal current channels can be a significant source of the radial component of the magnetic field in the photosphere. The roots of these coronal current channels in the photosphere are the source of the magnetic field component parallel to the polarity inversion line in active region NOAA 12673. These analyses and observations transform our theoretical understanding of coronal evolution and argue for a reexamination of the present paradigm in which the convection zone is the sole source of the photospheric magnetic field.

Keywords: Magnetic fields(994) — Solar magnetic fields(1503) — Solar photosphere(1518) — Magnetohydrodynamics(1964) — Solar coronal mass ejections(310)

1. INTRODUCTION

The sun constantly produces bare or partially dressed direct current channels, where in the latter case sheath currents provide incomplete shielding for the direct current. The sun's dipole magnetic field, which reverses approximately every 11 yr, and potential fields in the photosphere are manifestations of bare or partially dressed current systems in the solar interior. In the former case the sun's dipole magnetic field is inevitably carried by the solar wind to the edge of the solar system and then beyond the heliopause by interstellar flows. While the interior of the sun regularly produces bare currents on the scale of the heliosphere, a prevailing solar school of thought, based on arguments presented in Parker (1996a,b), is that the corona cannot produce or maintain a bare current. Thus, all coronal currents must be locally counterbalanced—direct currents must be perfectly sheathed on small scales and thus the corona cannot maintain net currents on large scales. This position largely follows from a fibril property of coronal magnetic fields that is assumed, and in some situations, observed to structure the solar atmosphere (Piddington 1978; Zwaan 1978; Parker 1984; Zwaan 1985; Vishniac 1995). In particular, assuming a fibril coronal structure leads to the conclusion that "Only the 'microscopic' internal structure of the individual fibril involves currents, and the longitudinal total [current] for any individual separate fibril is zero" (Parker 1996b). A current system with a balanced direct and sheath current (sometimes termed a *return current*) that produces no magnetic field beyond the outer edge of the sheath current is termed *neutral* or *neutralized.* This paradigm of the solar magnetic field structured by perfectly isolated and current balanced magnetic fibrils is in direct contradiction to the concept of a potential field in the corona. Strictly speaking, an ideal potential field does not carry current, nor is it isolated—and its mere existence requires a bare or partially dressed current system outside the region of interest. Indeed, the emergence of a potential active region (AR) requires the emergence of a precursor bare sheath current system that initially shields the corona from the long range potential field produced by the direct current in the convection zone. The counterbalancing contributions from both the direct and sheath currents may indeed largely cancel beyond the edge of the sheath current, although certainly a detailed cancelation cannot be perfect and high order magnetic multipoles must eventually radiate into the heliosphere.

peter.schuck@nasa.gov

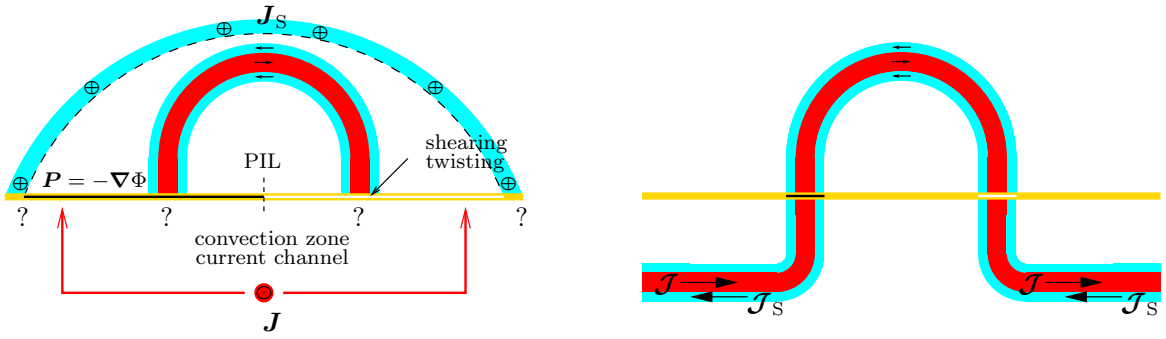

Figure 1. Schematic diagram of (left) kinematic and (right) dynamic formation of non-potential ARs. The left panel displays a potential field $\boldsymbol{P}$ produced by a bare direct current $\boldsymbol{J}$ below the photosphere, which imposes a dipole structure indicated by the negative (black) and positive (white) footpoints and the PIL in the photosphere (gold). Beyond the dashed line the ambient corona is shielded from the potential field by a counterbalancing sheath current $\boldsymbol{J}_S$. Kinematic shearing of this potential field results in the development of an arched direct (red) and sheath (cyan) current across the PIL in the plane of the diagram. The right panel displays the dynamic emergence of counterbalancing direct $\boldsymbol{\mathcal{J}}$ (red) and sheath $\boldsymbol{\mathcal{J}}_S$ (cyan) currents. The neutralized current system is also assumed to support some axial field, as indicated by the negative (black) and positive (white) footpoints in the photosphere. The question marks in the left panel indicate that this type of scenario does not address how the currents connect in the convection zone.

Consequently, the emergence of a potential field inevitably produces a bare sheath current in the corona and a bare direct current in the convection zone that is ultimately the source of a potential field between the two current systems in the corona. If one accepts the existence of a true potential field in the corona, then one must also accept that bare or partially dressed direct and sheath currents exist and are indeed necessary for the emergence of a potential field. Once the concept of isolated magnetic fibrils structuring the solar atmosphere is relaxed, the operative questions move from the existence of bare currents to the scale and character of the magnetic fields produced by these current systems, which is the subject of this article.

Another prevailing paradigm is that the convection zone is the origin of the radial magnetic field B_r observed in the photosphere. Indeed, this component of the photospheric field is often termed the *emerged field* (Schrijver & Zwaan 2000; Hagenaar 2001; Cheung et al. 2008; Fan 2009; MacTaggart 2011; Otsuji et al. 2011; Toriumi et al. 2014; Norton et al. 2017; Fan & Liu 2019) indicating that the photospheric field's immutable source is philosophically in the convection zone, not the chromosphere or corona. However, the radial field B_r in the photosphere is partly produced by chromospheric and coronal currents—this signature is unambiguously quantifiable and coherent in the photosphere and unequivocally demonstrates that convection zone, chromospheric, and coronal currents are at best partially dressed.

Two idealized scenarios exist for the emergence of non-potential ARs (Cheung & Isobe 2014). In one scenario, ARs emerge as potential fields, and then sheared arcades and flux ropes are produced by kinematic shearing and flux canceling flows (McClymont & Fisher 1989; Klimchuk & Sturrock 1992; Aulanier et al. 2010). In the alternative scenario, coronal structure dynamically emerges through the photosphere as twisted current-carrying magnetic flux tubes—ARs are born non-potential (Kurokawa 1991; Tanaka 1991; Melrose 1995; Leka et al. 1996; Fan 2001). Of course, in either case, the convection zone flows are ultimately the source of the current systems that energize the coronal magnetic fields. Dalmasse et al. (2015) note that both of these paradigms should produce shielded coronal current systems, e.g., twisted flux ropes carrying a direct current in their central core, which is embedded in a sheath current that shields the ambient plasma (see, e.g., Figure 3 in Melrose 1991).

For example, the left panel of Figure 1 shows a schematic diagram of a potential field $\boldsymbol{P} = -\nabla\Phi$ produced by the bare direct current $\boldsymbol{J}$ (colored red and out of the page) in the convection zone. Initially, the ambient corona must be shielded from this potential field by a counterbalancing sheath current $\boldsymbol{J}_S$ (colored cyan and into the page beyond the dashed arch). The potential field $\boldsymbol{P}$ between the bare current and the sheath current imposes a magnetic structure on the photosphere (gold) as indicated by the negative (black) and positive (white) footpoints separated by the polarity inversion line (PIL). This potential field $\boldsymbol{P}$ is kinematically locally twisted and sheared by flows in the photosphere to produce a neutralized current system along the arch in the plane of the diagram that connects the negative and positive polarities rooted in the photosphere. This scenario largely ignores the connectivity in the convection zone, as symbolized by the question marks in the figure, and usually assumes that the sheath current at the edge of the potential field has either dissipated or moved to such large distances as to be of negligible effect on the evolution of

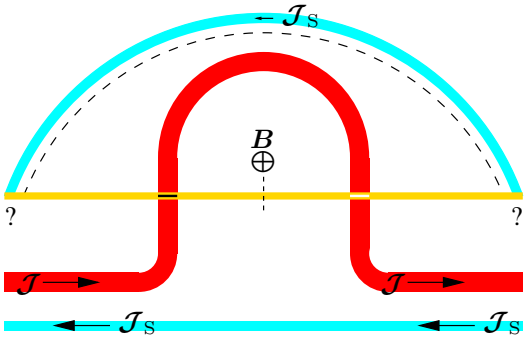

Figure 2. Schematic of a direct current ($\boldsymbol{\mathcal{J}}$, red) where the counterbalancing sheath currents ($\boldsymbol{\mathcal{J}}_S$, cyan) become detached from the direct current, such that the local corona, convection zone, and photosphere respond to the direct current as effectively a bare current. The direct current channel is assumed to support some axial field, as indicated by the negative (black) and positive (white) footpoints in the photosphere (gold). Question marks indicate that the sheath current connects in some unspecified manner to the convection zone current.

the AR. Alternatively, a direct current $\boldsymbol{\mathcal{J}}$ (red) may emerge dynamically through the photosphere in an idealized state shielded by a counterbalancing sheath current $\boldsymbol{\mathcal{J}}_S$ (cyan), as shown in the right panel of Figure 1. Presumably this current system also carries some axial flux, as indicated by the negative (black) and positive (white) footpoints in the photosphere (gold). The sheath current is ideally assumed to perfectly shield the direct current, and thus the ambient corona is insulated from the evolution of the emerged current system.

Regardless of the process for generating a non-potential but neutralized current system in the corona either by kinematic flows in the photosphere or dynamic flux emergence from the convection zone, these systems are not required to remain locally isolated in the corona because the system has emerged from a high $\beta = 8\pi p/B^2$ plasma in the convection zone and photosphere into a low β plasma in the corona and thus the forces have changed from pressure dominated ($\boldsymbol{\nabla} p$) to Lorentz force dominated ($\boldsymbol{J} \times \boldsymbol{B}$). Indeed, the sheath current may become detached from the direct current in the corona, as shown schematically in Figure 2, and then these oppositely directed current systems will repel each other until they reach a new equilibrium with each other and their surroundings resulting in distinct $\boldsymbol{\mathcal{J}}$ and $\boldsymbol{\mathcal{J}}_S$ current channels. The redistribution of the currents in the corona can produce direct and sheath current systems that are effectively bare on scales smaller than the flux system enclosing each of them even if they are counterbalancing on larger scales of order the radius of the sun $\lesssim R_\odot$.

Nonetheless, the existence of bare current channels in the corona remains controversial (Melrose 1991, 1995; Parker 1996b; Melrose 1996, 2017). Two major challenges complicate the controversy. The first is the definition of a bare current—a counterbalancing current may always exist beyond the local measurements available to the observer, i.e., the sheath current shown in the left panel of Figure 1. One popular observational approach to attempt to discriminate between locally bare and locally balanced current systems is to measure the net integrated normal current in the polarities of ARs. Statistical (Wheatland 2000; Kontogiannis et al. 2017; Fursyak et al. 2020) and event (Georgoulis et al. 2012; Gosain et al. 2014; Liu et al. 2017) studies have largely concluded that some AR polarities support a net current and others support counterbalancing currents. However, these studies have not changed the conventional picture of coronal currents, perhaps because of the second major challenge in this controversy, namely, that determining the net current over partitions of positive and negative magnetic polarities in the photosphere is fraught with observational challenges. This approach (i) must determine the PIL accurately where the signal to noise in B_r is significant, and (ii) involves the differentiation of the noisy and/or corrupted[1] tangential components of $\boldsymbol{B}$ to compute the radial current J_r or involves the integration of the noisy and/or corrupted tangential component of $\boldsymbol{B}$ around the noisy PIL via Stokes' theorem. Consequently, the inherent biases and uncertainties in vector magnetograms complicate unambiguously distinguishing flux systems that support counterbalancing current systems from ones that support net currents. Nevertheless, recent analysis of magnetohydrodynamic (MHD) simulations by Török et al. (2014) and Dalmasse et al. (2015) lend support to observations of emerging ARs with polarities that carry a net current. Dalmasse et al. (2015) further demonstrated that photospheric shearing can produce net currents in the solar corona. Another possible signature of a bare current that is quantifiable with vector field measurements is illustrated in Figure 2: a bare current produces a net magnetic

[1] The identification and repair of corrupted pixels will be discussed in § 4 and Appendix A.

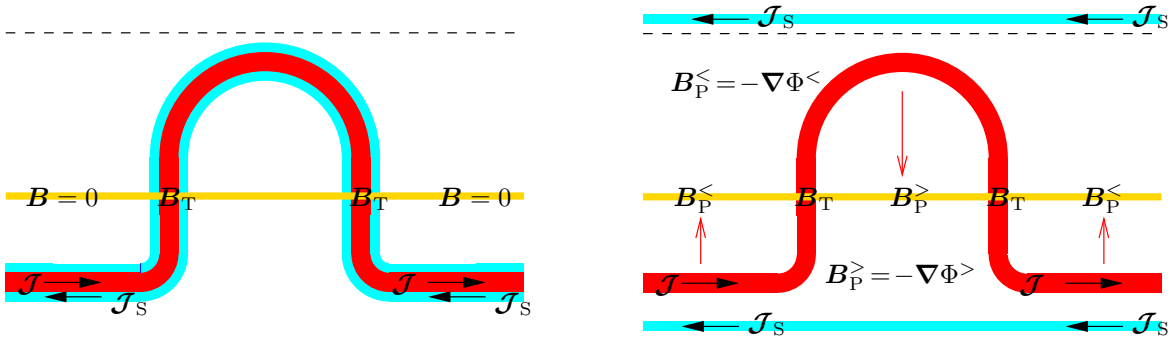

Figure 3. Schematic diagram of the magnetic field components from the CICCI calculation superimposed on illustrative current systems. The left panel displays the balanced and perfectly shielded current system from the right panel of Figure 1 and the right panel displays the partially dressed currents from Figure 2. The red arrows indicate the sources of $\boldsymbol{B}_\mathrm{P}^{<}$ and $\boldsymbol{B}_\mathrm{P}^{>}$, and the symbols $\boldsymbol{B}_\mathrm{T}$ are placed on their sources, the radial currents J_r passing through the photosphere.

field (into the page) between the roots of the current system in the photosphere. If the vertical dashed line between the roots of the current system corresponds to a PIL, then this scenario directly and naturally produces a component of a magnetic field parallel to the PIL. Regardless of the strict definition of the bare current, perfect shielding of the photosphere from any detectable magnetic signature of convection zone, coronal, and chromospheric current systems is implausible and thus the signature of these atmospheric currents should be detectable in the photosphere as these systems will only be partially dressed even if they are not strictly bare. Indeed, this article demonstrates that the magnetic fingerprints of these partially dressed currents do indeed exist and can be detected in the photosphere. Thus, this article focuses on the origin of the components of the magnetic field in the photosphere.

This article is organized as follows: § 2 introduces the magnetic field decomposition $\boldsymbol{B}=\boldsymbol{B}_\mathrm{P}^{<}+\boldsymbol{B}_\mathrm{P}^{>}+\boldsymbol{B}_\mathrm{T}$ on a sphere due to Gauß (1839). This analysis of the photospheric magnetic field, termed Carl's (Gauß) Indirect Coronal Current Imager (CICCI) imposes no preconceived assumptions regarding the current sources of the photospheric magnetic field and quantitatively determines the magnetic components produced by currents below the photosphere $\boldsymbol{B}_\mathrm{P}^{<}$, above the photosphere $\boldsymbol{B}_\mathrm{P}^{>}$, and through the photosphere $\boldsymbol{B}_\mathrm{T}$. This decomposition of the photospheric magnetic field into three unique components, one of which $\boldsymbol{B}_\mathrm{P}^{>}$ may be unambiguously associated with current systems in the corona, immediately raises paradigm shifting questions with universal impact across observation, theory, and modeling, and space-weather forecasting. § 3 validates CICCI by leveraging the full 3D data cube produced by MHD simulations to connect the magnetic signatures revealed by CICCI analysis of the simulation lower boundary (photosphere) with material current systems within the simulation volume (corona). § 4 applies CICCI to Solar Dynamics Observatory/Helioseismic and Magnetic Imager (SDO/HMI) observations of AR 12673 to reveal the current systems in the chromosphere/corona. For the remainder of this article we use *corona* to generically refer to the solar atmosphere above the photosphere, namely, the *chromosphere, transition region, and corona.*

2. CARL'S (Gauß) INDIRECT CORONAL CURRENT IMAGER (CICCI)

The origin of the magnetic field $\boldsymbol{B}(\boldsymbol{x})$ is in nonlocal current sources $\boldsymbol{J}(\boldsymbol{x}')$ elsewhere in space (Biot & Savart 1820). Therefore, an inherently nonlocal analysis is required to determine the origin of the magnetic field at a specific location in space. The CICCI analysis combines the Helmholtz-Hodge decomposition of a vector field on a surface, the solenoidal property of the magnetic field, and vector spherical harmonics with Gauß's (1839) insight that the magnetic field on a closed spherical surface $\mathcal{S}(r=R_\odot)$ such as the photosphere may be uniquely decomposed into three components: $\boldsymbol{B}=\boldsymbol{B}_\mathrm{P}^{<}+\boldsymbol{B}_\mathrm{P}^{>}+\boldsymbol{B}_\mathrm{T}$. Here the subscripts "P" and "T" indicate the poloidal and toroidal components of the magnetic field, respectively, and the superscripts "<" and ">" indicate the region of space containing the current system that produces $\boldsymbol{B}_\mathrm{P}$: (i) $\boldsymbol{B}_\mathrm{P}^{<}$ is the poloidal component produced by current sources $\boldsymbol{J}$ below the photosphere (in the convection zone $r<R_\odot$) which is intrinsically potential above the photosphere (in the corona $r>R_\odot$); (ii) $\boldsymbol{B}_\mathrm{P}^{>}$ is the poloidal component produced by current sources $\boldsymbol{J}$ above the photosphere (in the corona $r>R_\odot$), which is intrinsically potential below the photosphere (in the convection zone $r<R_\odot$); and (iii) $\boldsymbol{B}_\mathrm{T}$ is the toroidal component produced by currents passing through the photosphere $r=R_\odot$, where $\boldsymbol{B}_\mathrm{T}\cdot\hat{\boldsymbol{r}}=0$. Figure 3 shows a schematic diagram of the magnetic field components from the CICCI calculation and their relationship to current sources. The left panel of Figure 3 displays the balanced and perfectly shielded current system from the right panel of Figure 1, and

the right panel of Figure 3 displays the partially dressed currents from Figure 2. Using the CICCI decomposition, the two paradigms of perfectly shielded and partially dressed current systems may be unambiguously distinguished with vector magnetic field observations. Here, the red arrows indicate the sources of $\boldsymbol{B}_{\rm P}^{<}$ and $\boldsymbol{B}_{\rm P}^{>}$, and the symbols $\boldsymbol{B}_{\rm T}$ are placed on their sources, the radial currents J_r passing through the photosphere.

2.1. *Mathematical Foundations of CICCI*

The mathematical foundations of CICCI require the introduction of some basic vector calculus on a spherical surface $\mathcal{S}(r)$. An arbitrary vector $\boldsymbol{B}$ may be written as a Helmholtz-Hodge decomposition in spherical geometry (r,ϑ,φ) (Backus 1986)

$$\boldsymbol{B}(\boldsymbol{x}) = \overbrace{Q(r,\vartheta,\varphi)\,\hat{\boldsymbol{r}} + \underbrace{r\,\boldsymbol{\nabla}_{\mathcal{S}} S(r,\vartheta,\varphi)}_{\boldsymbol{B}_{\mathcal{S}}}}^{\boldsymbol{B}_{\rm P}\text{ (poloidal)}} + \overbrace{\boldsymbol{\nabla}\times[\hat{\boldsymbol{r}}\,r\,T(r,\vartheta,\varphi)]}^{\boldsymbol{B}_{\rm T}\text{ (toroidal)}}. \tag{1a}$$

For a solenoidal field this may also be expressed as the poloidal-toroidal decomposition (Chandrasekhar 1961)

$$\boldsymbol{B}(\boldsymbol{x}) = \underbrace{\boldsymbol{\nabla}\times\{\boldsymbol{\nabla}\times[\hat{\boldsymbol{r}}\,r\,P(r,\vartheta,\varphi)]\}}_{\boldsymbol{B}_{\rm P}\text{ (poloidal)}} + \underbrace{\boldsymbol{\nabla}\times[\hat{\boldsymbol{r}}\,r\,T(r,\vartheta,\varphi)]}_{\boldsymbol{B}_{\rm T}\text{ (toroidal)}}, \tag{1b}$$

where Q, S, T, and P are the radial, spheroidal, toroidal, and poloidal scalar fields, respectively, and

$$\boldsymbol{\nabla}_{\mathcal{S}} \equiv \boldsymbol{\nabla} - \hat{\boldsymbol{n}}\,(\hat{\boldsymbol{n}}\cdot\boldsymbol{\nabla}) = \hat{\boldsymbol{\vartheta}}\,\frac{1}{r}\,\frac{\partial}{\partial\vartheta} + \hat{\boldsymbol{\varphi}}\,\frac{1}{r\,\sin\vartheta}\,\frac{\partial}{\partial\varphi}, \tag{2}$$

is the surface gradient operator, which is defined as tangent to the normal $\hat{\boldsymbol{n}} = \hat{\boldsymbol{r}}$ of the spherical surface $\mathcal{S}(r)$. The solenoidal property of the magnetic field ($\boldsymbol{\nabla}\cdot\boldsymbol{B} = 0$) implies that S and P are related by

$$S(r,\vartheta,\varphi) = \frac{1}{r}\,\frac{\partial\,[r\,P(r,\vartheta,\varphi)]}{\partial r}. \tag{3}$$

For a solenoidal field, such as the magnetic field, the first two terms in (1a) are the components of the poloidal field $\boldsymbol{B}_{\rm P}$ and the third term is the toroidal field $\boldsymbol{B}_{\rm T}$. The poloidal-toroidal representation, (1a)-(1b), decomposes the surface vector field $\boldsymbol{B}_{\mathcal{S}} \equiv \boldsymbol{B} - \hat{\boldsymbol{n}}\,(\hat{\boldsymbol{n}}\cdot\boldsymbol{B})$, i.e., the components of $\boldsymbol{B}$ that lie in the surface $\mathcal{S}(r)$, into two vectors with distinct characteristics, as they are orthogonal $\oint_{\mathcal{S}(r)} d\varphi\,d\vartheta\,\sin\vartheta\,\boldsymbol{B}_{\rm T}\cdot\boldsymbol{B}_{\rm P}$=0. For a closed contour $\mathcal{C}$ that lies in a spherical surface $\mathcal{S}(r)$, the poloidal field $\boldsymbol{B}_{\rm P}$ is conservative and the toroidal field $\boldsymbol{B}_{\rm T}$ is related to the radial displacement $c^{-1}\partial E_r/\partial t$ and material J_r currents through the area $\mathcal{A}$ enclosed by $\mathcal{C}$ by Stokes' theorem, with $\mathcal{C}\in\mathcal{S}$, $\mathcal{A}\in\mathcal{S}$, and $\mathcal{C}$ enclosing $\mathcal{A}$:

$$\oint_{\mathcal{C}} d\boldsymbol{l}\cdot\boldsymbol{B}_{\rm P} = 0, \tag{4a}$$

$$\oint_{\mathcal{C}} d\boldsymbol{l}\cdot\boldsymbol{B}_{\rm T} = \int_{\mathcal{A}} dS\,\hat{\boldsymbol{r}}\cdot\boldsymbol{\nabla}\times\boldsymbol{B} = \int_{\mathcal{A}} dS\,\hat{\boldsymbol{r}}\cdot\left[\frac{1}{c}\,\frac{\partial\boldsymbol{E}}{\partial t} + \frac{4\,\pi}{c}\,\boldsymbol{J}\right]. \tag{4b}$$

In the quasistatic limit $\partial\boldsymbol{E}/\partial t \approx 0$, the structures in $\boldsymbol{B}_{\rm T}$ are direct indications of radial current systems J_r through the surface $\mathcal{S}(r)$ because (i) all field lines of the toroidal field $\boldsymbol{B}_{\rm T}$ must close on $\mathcal{S}(r)$: $\hat{\boldsymbol{r}}\cdot\boldsymbol{B}_{\rm T} = 0$ everywhere and (ii) conversely, the field lines of $\boldsymbol{B}_{\rm P}$ cannot close anywhere on $\mathcal{S}(r)$: $\hat{\boldsymbol{r}}\cdot\boldsymbol{\nabla}\times\boldsymbol{B}_{\rm P} = 0$ everywhere. Both of these clauses together imply that if one can estimate $\boldsymbol{B}_{\rm T}$ on $\mathcal{S}(R_\odot)$ there is no need to estimate J_r to unambiguously demonstrate the presence of a radial current system passing through the photosphere at $r = R_\odot$, i.e., a toroidal field is a necessary and sufficient condition for a radial current through $\mathcal{S}(R_\odot)$. The second clause implies that the poloidal field $\boldsymbol{B}_{\rm P}$ is produced by toroidal current systems

$$\boldsymbol{J}_{\rm T} = (4\,\pi)^{-1}\,c\,\boldsymbol{\nabla}\times\left[\hat{\boldsymbol{r}}\,r\,\nabla^2 P(r,\vartheta,\varphi)\right], \tag{5}$$

which are always tangent to spherical surfaces $\mathcal{S}(r)$. This tangential nature of the toroidal current system $\boldsymbol{J}_{\rm T}$ is useful for separating the poloidal magnetic field $\boldsymbol{B}_{\rm P}$ into $\boldsymbol{B}_{\rm P}^{<}$ and $\boldsymbol{B}_{\rm P}^{>}$.

The poloidal-toroidal decomposition also provides formally simple differential relationships between the scalars Q, S, and T and vector properties of particular interest to analysis in the surface $\mathcal{S}(r)$:

$$\text{radial field} = \hat{\boldsymbol{n}} \cdot \boldsymbol{B} = \hat{\boldsymbol{n}} \cdot \boldsymbol{B}_{\mathrm{P}} = Q = -r\,\nabla^2_{\mathcal{S}} P = B_r, \tag{6a}$$

$$\text{surface divergence} = \boldsymbol{\nabla}_{\mathcal{S}} \cdot \boldsymbol{B} = \boldsymbol{\nabla}_{\mathcal{S}} \cdot \boldsymbol{B}_{\mathcal{S}} + \frac{2\,B_r}{r} = \boldsymbol{\nabla}_{\mathcal{S}} \cdot \boldsymbol{B}_{\mathrm{P}} = r\,\nabla^2_{\mathcal{S}} S + \frac{2\,B_r}{r} = -\frac{\partial B_r}{\partial r}, \tag{6b}$$

$$\text{surface curl} = \hat{\boldsymbol{n}} \cdot \boldsymbol{\nabla} \times \boldsymbol{B} = \hat{\boldsymbol{n}} \cdot \boldsymbol{\nabla}_{\mathcal{S}} \times \boldsymbol{B}_{\mathcal{S}} = \hat{\boldsymbol{n}} \cdot \boldsymbol{\nabla}_{\mathcal{S}} \times \boldsymbol{B}_{\mathrm{T}} = -r\,\nabla^2_{\mathcal{S}} T = \hat{\boldsymbol{r}} \cdot \left[\frac{1}{c}\frac{\partial \boldsymbol{E}}{\partial t} + \frac{4\,\pi}{c}\boldsymbol{J} \right], \tag{6c}$$

where

$$\boldsymbol{\nabla}_{\mathcal{S}} \cdot \boldsymbol{B} = \boldsymbol{\nabla} \cdot \boldsymbol{B} - \hat{\boldsymbol{n}} \cdot \frac{\partial \boldsymbol{B}}{\partial n}, \tag{7}$$

is the surface divergence and

$$\nabla^2_{\mathcal{S}} = \frac{1}{r^2\,\sin\vartheta}\frac{\partial}{\partial\vartheta}\left(\sin\vartheta\frac{\partial}{\partial\vartheta}\right) + \frac{1}{r^2\,\sin^2\vartheta}\frac{\partial^2}{\partial\varphi^2}, \tag{8}$$

is the Laplace-Beltrami operator on a sphere. The surface divergence, Equation (6b), and surface curl, Equation (6c), are also related to physical properties such as the radial variation of the radial field and the radial component of the Ampére-Maxwell relation, respectively, where $\boldsymbol{E}$ is the electric field and $\boldsymbol{J}$ is the material current density. For a closed spherical surface $\mathcal{S}(r)$ the relationships Equations (6a)-(6c) uniquely determine the scalars S, T, P, and Q to within meaningless constants through the Laplace-Beltrami equation (Poisson's equation $\nabla^2_{\mathcal{S}}\psi = \varrho$ on a sphere).

2.2. *Vector Spherical Harmonic Decomposition of Magnetic Fields*

Gauß's (1839) insight may be illuminated by combining vector calculus on a sphere and the solenoidal property of the magnetic field with (vector) spherical harmonics. The relationships provided by Equations (3) and (6a)--(6c) may be solved in physical space $\boldsymbol{x}$ for Q, S, T, P, and $\partial P/\partial r$ given the vector magnetic fields prescribed on a single spherical surface $\mathcal{S}(R_\odot)$. However, this approach (i) could amplify any noise in the magnetic field data because it requires computation of the radial component of the current J_r from $\boldsymbol{B}_{\mathcal{S}}$ (perhaps by finite differences) and (ii) does not produce a simple separation of poloidal fields into $\boldsymbol{B}^{<}_{\mathrm{P}}$ and $\boldsymbol{B}^{>}_{\mathrm{P}}$ produced by sources interior ($r < R$) and exterior ($r > R$) to the spherical surface $\mathcal{S}(R_\odot)$. Alternatively, global spectral methods have attractive properties for attribution of the magnetic field to sources: (i) this approach is explicitly nonlocal, the solution at any point $\boldsymbol{x}$ depends not only on information at neighboring points, but on information from the entire surface $\mathcal{S}(r)$—thus the variables Q, S, T, P, and $\partial P/\partial r$ are connected nonlocally; (ii) this method converges exponentially fast and is more accurate than finite-difference solutions when the solution is smooth. Spectral methods are frequently implemented to perform potential field source surface extrapolations that are commonly used throughout the solar physics community (Altschuler & Newkirk 1969; Schatten et al. 1969; Hoeksema 1984; Wang & Sheeley 1992).

To apply spectral methods to Equations (6a)-(6c) we seek a representation that diagonalizes the Laplace-Beltrami operator, Equation (8), on a closed spherical surface $\mathcal{S}(r)$ of constant radius r which will reduce the differential relationships in Equations (6a)-(6c) to algebraic ones. This is provided by the scalar spherical harmonic transform (SSHT) defined as

$$f(\boldsymbol{x}) = \sum_{\ell=0}^{\infty}\sum_{m=-\ell}^{\ell} \widetilde{f}_{\ell,m}(r)\,\mathrm{Y}_{\ell,m}(\vartheta,\varphi), \tag{9}$$

where

$$\mathrm{Y}_{\ell,m}(\vartheta,\varphi) \equiv \sqrt{\frac{2\,\ell+1}{4\,\pi}\frac{(\ell-m)!}{(\ell+m)!}}\,\mathrm{P}^m_\ell(\cos\vartheta)\,e^{i\,m\,\varphi}, \tag{10}$$

is the scalar spherical harmonic and P^m_ℓ is the associated Legendre function of degree ℓ and order m

$$\mathrm{P}^m_\ell(x) = \frac{(-1)^m}{2^\ell\,\ell!}\left(1-x^2\right)^{m/2}\frac{d^{\ell+m}}{dx^{\ell+m}}\left(x^2-1\right)^\ell. \tag{11}$$

The scalar spherical harmonics are eigenfunctions of and thus diagonalize the Laplace-Beltrami operator (8) on a closed spherical surface $\mathcal{S}(r)$

$$\nabla^2_{\mathcal{S}}\,\mathrm{Y}_{\ell,m}(\vartheta,\varphi) = -\frac{\ell\,(\ell+1)}{r^2}\,\mathrm{Y}_{\ell,m}(\vartheta,\varphi). \tag{12}$$

The scalar spherical harmonics have the desirable properties of orthogonality

$$\int_0^{2\,\pi} d\varphi \int_0^{\pi} d\vartheta \, \sin\vartheta \; \mathrm{Y}^*_{\ell',m'}\left(\vartheta,\varphi\right) \, \mathrm{Y}_{\ell,m}\left(\vartheta,\varphi\right) = \delta_{\ell',\ell}\,\delta_{m',m}, \tag{13a}$$

and completeness

$$\sum_{\ell=0}^{\infty}\sum_{m=-\ell}^{\ell} \mathrm{Y}^*_{\ell,m}\left(\vartheta',\varphi'\right) \, \mathrm{Y}_{\ell,m}\left(\vartheta,\varphi\right) = \delta\left(\cos\vartheta' - \cos\vartheta\right) \, \delta\left(\varphi' - \varphi\right), \tag{13b}$$

on $\mathcal{S}\left(r\right)$ where $\delta_{i,j}$ is the Kronecker delta and $\delta\left(x\right)$ is the Dirac delta distribution.

Expanding Q, S, T, and P in scalar spherical harmonics[2] produces the vector spherical harmonic decomposition

$$\boldsymbol{B}\left(\boldsymbol{x}\right) = \sum_{\ell=1}^{\infty}\sum_{m=-\ell}^{\ell}\left[\widetilde{Q}_{\ell,m}\left(r\right) \, \mathbf{Y}_{\ell,m}\left(\vartheta,\varphi\right) + \widetilde{S}_{\ell,m}\left(r\right) \, \boldsymbol{\Psi}_{\ell,m}\left(\vartheta,\varphi\right) - \widetilde{T}_{\ell,m}\left(r\right) \, \boldsymbol{\Phi}_{\ell,m}\left(\vartheta,\varphi\right)\right] \tag{14a}$$

$$= \boldsymbol{\nabla}\times\sum_{\ell=1}^{\infty}\sum_{m=-\ell}^{\ell}\left\{\boldsymbol{\nabla}\times\left[r\,\widetilde{P}_{\ell,m}\left(r\right) \, \mathbf{Y}_{\ell,m}\left(\vartheta,\varphi\right)\right] + r\,\widetilde{T}_{\ell,m}\left(r\right) \, \mathbf{Y}_{\ell,m}\left(\vartheta,\varphi\right)\right\}, \tag{14b}$$

where the second expression is manifestly divergence-free and $\widetilde{Q}_{\ell,m}(r)$, $\widetilde{S}_{\ell,m}(r)$, $\widetilde{P}_{\ell,m}(r)$ and $\widetilde{T}_{\ell,m}(r)$ are the SSHT coefficients of the radial, spheroidal, poloidal, and toroidal scalars, respectively. The basis vectors

$$\mathbf{Y}_{\ell,m}\left(\vartheta,\varphi\right) \equiv \mathrm{Y}_{\ell,m}\left(\vartheta,\varphi\right)\,\hat{\boldsymbol{r}}, \qquad \boldsymbol{\Psi}_{\ell,m}\left(\vartheta,\varphi\right) \equiv r\,\boldsymbol{\nabla}\,\mathrm{Y}_{\ell,m}\left(\vartheta,\varphi\right), \qquad \text{and} \qquad \boldsymbol{\Phi}_{\ell,m}\left(\vartheta,\varphi\right) \equiv \hat{\boldsymbol{r}}\times\,r\,\boldsymbol{\nabla}\,\mathrm{Y}_{\ell,m}\left(\vartheta,\varphi\right), \tag{15}$$

are the vector spherical harmonics (Morse & Feshbach 1953; Barrera et al. 1985). The coefficients of the expansion in Eq. (14a) at any spherical surface $\mathcal{S}\left(r\right)$ are given by the vector spherical harmonic transforms (VSHTs) on that surface

$$\widetilde{Q}_{\ell,m}\left(r\right) = \int d\Omega\,\boldsymbol{B}\left(r,\vartheta,\varphi\right)\cdot\mathbf{Y}^*_{\ell,m}\left(\vartheta,\varphi\right), \tag{16a}$$

$$\widetilde{S}_{\ell,m}\left(r\right) = \frac{1}{\ell\left(\ell+1\right)}\int d\Omega\,\boldsymbol{B}\left(r,\vartheta,\varphi\right)\cdot\boldsymbol{\Psi}^*_{\ell,m}\left(\vartheta,\varphi\right), \tag{16b}$$

$$\widetilde{T}_{\ell,m}\left(r\right) = \frac{-1}{\ell\left(\ell+1\right)}\int d\Omega\,\boldsymbol{B}\left(r,\vartheta,\varphi\right)\cdot\boldsymbol{\Phi}^*_{\ell,m}\left(\vartheta,\varphi\right), \tag{16c}$$

where $\boldsymbol{B}$ is the observed magnetic field, "$*$" denotes the complex conjugate and $d\Omega = d\varphi\,d\vartheta\,\sin\vartheta$ is the solid angle. The determination of Q, S, and particularly T via VSHTs does not require any differentiation of the spatial data representing $\boldsymbol{B}\left(\boldsymbol{x}\right)$ on $\mathcal{S}\left(r\right)$. These coefficients are determined directly from the vector properties of the magnetic field in the photosphere.

The solenoidal property of the magnetic field ($\boldsymbol{\nabla}\cdot\boldsymbol{B} = 0$) also relates the (spectral) coefficients $\widetilde{Q}_{\ell,m}\left(r\right)$, $\widetilde{S}_{\ell,m}\left(r\right)$ and $\widetilde{P}_{\ell,m}\left(r\right)$ in Equations (14a)-(14b) by

$$\widetilde{Q}_{\ell,m}\left(r\right) = \frac{\ell\,\left(\ell+1\right)}{r^2}\,\left[r\,\widetilde{P}_{\ell,m}\left(r\right)\right], \tag{17a}$$

$$\widetilde{S}_{\ell,m}\left(r\right) = \frac{1}{r}\,\frac{\partial\left[r\,\widetilde{P}_{\ell,m}\left(r\right)\right]}{\partial r}. \tag{17b}$$

[2] We emphasize that the SSHT is applied to the scalars Q, S, T, and P, and not directly to the components of $\boldsymbol{B}$. Applying the SSHT directly on the individual vector components $(B_r, B_\vartheta, B_\varphi)$ on $\mathcal{S}\left(r\right)$ might naively appear to be the best mathematical path forward to produce simple algebraic or ordinary differential relationships between the magnetic field and vector field properties on $\mathcal{S}\left(r\right)$. Unfortunately, this straightforward approach does not succeed at producing simple intuitive relationships between the coefficients $\widetilde{B}_{\vartheta\,\ell,m}\left(r\right)$ and $\widetilde{B}_{\varphi\,\ell,m}\left(r\right)$ of Equation (9) applied to the components of $\boldsymbol{B}_{\mathcal{S}}$ and surface vector field properties, Equations (6b)-(6c) on a sphere $\mathcal{S}\left(r\right)$, e.g., $\boldsymbol{\nabla}_{\mathcal{S}}\cdot\boldsymbol{B} = -\partial B_r/\partial r$. Note that spherical harmonics $\mathrm{Y}_{\ell,m}$ are representations of the special orthogonal symmetry group SO(3) of rotations about the origin. Scalars, such as $f\left(\boldsymbol{x}\right)$ in Equation (9), are physical quantities that are invariant under transformations to their vector space basis. For example, under the rotation matrix $\mathbb{R}$ and its transpose $\mathbb{R}^\dagger = \mathbb{R}^{-1}$ a scalar $f\left(\boldsymbol{x}\right) = \boldsymbol{g}^\dagger\left(\boldsymbol{x}\right)\cdot\boldsymbol{h}\left(\boldsymbol{x}\right)$, where $\boldsymbol{h}$ and $\boldsymbol{g}$ are ordinary vectors, transforms as $\boldsymbol{g}^\dagger\left(\boldsymbol{x}\right)\cdot\mathbb{R}^{-1}\cdot\mathbb{R}\cdot\boldsymbol{h}\left(\boldsymbol{x}\right) = \boldsymbol{g}^\dagger\left(\boldsymbol{x}\right)\cdot\boldsymbol{h}\left(\boldsymbol{x}\right) = f\left(\boldsymbol{x}\right)$. Thus representing a scalar as a superposition of elements of spherical harmonics of SO(3) reflects this rotational invariance. However, the components of vector fields are not invariant under SO(3). For example, the vector $\boldsymbol{B}\left(\boldsymbol{x}\right)$ under the rotation matrix $\mathbb{R}$ transforms as $\mathbb{R}\cdot\boldsymbol{B}\left(\boldsymbol{x}\right)$ which is not equivalent to the original vector $\boldsymbol{B}\left(\boldsymbol{x}\right)$. Thus, while describing the components of a vector field by a superposition of spherical harmonics is possible (as they form a complete basis), this description does not represent how vector fields transform under rotations (for an explicit example, see § 3 in Barrera et al. 1985).

Superficially comparing Equations (3) and (17b), there appears to be no immediate advantage to the spectral representation Equation (17b). Indeed, as noted above S, P, and $\partial P/\partial r$ may be uniquely specified by vector magnetic field data on $\mathcal{S}\left(R_\odot\right)$ and thus Equations (3) and (17b) appear to merely redundantly specify the radial derivative of the poloidal function or its spectral components, i.e., $\partial \widetilde{P}_{\ell,m}\left(r\right)/\partial r$, and does not facilitate separating the poloidal field into $\boldsymbol{B}_{\mathrm{P}}^{<}$ and $\boldsymbol{B}_{\mathrm{P}}^{>}$.

However, Gauß's (1839) insight is that the poloidal magnetic field $\boldsymbol{B}_{\mathrm{P}}$ could be uniquely decomposed into contributions from toroidal current sources ($\boldsymbol{J}_{\mathrm{T}}$ in Equation (5), which are tangential to spherical surfaces) interior and exterior to the Earth's surface (Glassmeier & Tsurutani 2014). Gauß realized that toroidal current sources in the exterior would produce a potential poloidal magnetic field $\boldsymbol{B}_{\mathrm{P}}^{>}$ in the interior and toroidal current sources in the interior would produce a potential poloidal $\boldsymbol{B}_{\mathrm{P}}^{<}$ magnetic field in the exterior. For attribution of photospheric magnetic fields to solar current systems, this physical insight for the poloidal field in the photosphere at $\mathcal{S}\left(R_\odot\right)$ becomes[3]

$$\widetilde{P}_{\ell,m}\left(r\right) = R_\odot\left[\widetilde{P}_{\ell,m}^{>}\left(r/R_\odot\right)^{\ell} + \widetilde{P}_{\ell,m}^{<}\left(R_\odot/r\right)^{\ell+1}\right], \tag{18}$$

where $\widetilde{P}_{\ell,m}^{<}$ represents the potential field in the photosphere due to current sources below the photosphere ($r < R_\odot$, e.g., in the convection zone), and $\widetilde{P}_{\ell,m}^{>}$ represents the potential field in the photosphere due to current sources above the photosphere ($r > R_\odot$, e.g., in the corona). This insight, combined with the two relationships (17a) and (17b), permits the poloidal coefficients $\widetilde{P}_{\ell,m}^{<}$ and $\widetilde{P}_{\ell,m}^{>}$ to be uniquely determined from the VSHT of the vector magnetic field in $\mathcal{S}\left(R_\odot\right)$ by substituting Equation (18) into Equations (17a) and (17b), producing

$$\widetilde{P}_{\ell,m}^{>} = \frac{\widetilde{Q}_{\ell,m}\left(R_\odot\right) + \left(\ell+1\right)\ \widetilde{S}_{\ell,m}\left(R_\odot\right)}{\left(\ell+1\right)\left(2\,\ell+1\right)}, \tag{19a}$$

$$\widetilde{P}_{\ell,m}^{<} = \frac{\widetilde{Q}_{\ell,m}\left(R_\odot\right) - \ell\,\widetilde{S}_{\ell,m}\left(R_\odot\right)}{\ell\left(2\,\ell+1\right)}. \tag{19b}$$

The corresponding coefficients for reconstruction of the fields on the surface $\mathcal{S}\left(R_\odot\right)$ from Eq. (14a) are

$$\widetilde{Q}_{\ell,m}^{<} = \ell\left(\ell+1\right)\widetilde{P}_{\ell,m}^{<}, \tag{20a}$$

$$\widetilde{Q}_{\ell,m}^{>} = \ell\left(\ell+1\right)\widetilde{P}_{\ell,m}^{>}, \tag{20b}$$

$$\widetilde{S}_{\ell,m}^{<} = -\,\ell\,\widetilde{P}_{\ell,m}^{<}, \tag{20c}$$

$$\widetilde{S}_{\ell,m}^{>} = \left(\ell+1\right)\widetilde{P}_{\ell,m}^{>}. \tag{20d}$$

The intrinsic components of the magnetic field at $r = R_\odot$ are synthesized with inverse VSHTs as

$$\boldsymbol{B}_{\mathrm{P}}^{<}\left(\vartheta,\varphi\right) = \sum_{\ell=1}^{\infty}\sum_{m=-\ell}^{\ell}\left[\ell\left(\ell+1\right)\widetilde{P}_{\ell,m}^{<}\,\mathbf{Y}_{\ell,m}\left(\vartheta,\varphi\right) - \ell\,\widetilde{P}_{\ell,m}^{<}\,\boldsymbol{\Psi}_{\ell,m}\left(\vartheta,\varphi\right)\right], \tag{21a}$$

$$\boldsymbol{B}_{\mathrm{P}}^{>}\left(\vartheta,\varphi\right) = \sum_{\ell=1}^{\infty}\sum_{m=-\ell}^{\ell}\left[\ell\left(\ell+1\right)\widetilde{P}_{\ell,m}^{>}\,\mathbf{Y}_{\ell,m}\left(\vartheta,\varphi\right) + \left(\ell+1\right)\widetilde{P}_{\ell,m}^{>}\,\boldsymbol{\Psi}_{\ell,m}\left(\vartheta,\varphi\right)\right], \tag{21b}$$

$$\boldsymbol{B}_{\mathrm{T}}\left(\vartheta,\varphi\right) = -\sum_{\ell=1}^{\infty}\sum_{m=-\ell}^{\ell}\widetilde{T}_{\ell,m}\,\boldsymbol{\Phi}_{\ell,m}\left(\vartheta,\varphi\right), \tag{21c}$$

where $\boldsymbol{B}_{\mathrm{P}}^{<}$ is the poloidal field in the photosphere produced by current sources in the convection zone, $\boldsymbol{B}_{\mathrm{P}}^{>}$ is the poloidal field in the photosphere produced by current sources in the corona, and $\boldsymbol{B}_{\mathrm{T}}$ is the toroidal field in the photosphere produced by radial current through the photosphere. The field $\boldsymbol{B}_{\mathrm{P}}^{<}$ is potential above the photosphere $r > R_\odot$ in the corona and $\boldsymbol{B}_{\mathrm{P}}^{>}$ is potential below the photosphere $r < R_\odot$ in the convection zone. Equations (21a)-(21c) reconstruct the magnetic field *exactly* in the photosphere, $\boldsymbol{B} = \boldsymbol{B}_{\mathrm{P}}^{<} + \boldsymbol{B}_{\mathrm{P}}^{>} + \boldsymbol{B}_{\mathrm{T}}$ with direct attribution to current

[3] This expression, which is a solution to Laplace's equation, describes the two potential components of the poloidal field $\boldsymbol{B}_{\mathrm{P}}^{<}$ and $\boldsymbol{B}_{\mathrm{P}}^{>}$ on $\mathcal{S}\left(R_\odot\right)$ in the absence of a singular surface current in the photosphere. This expression does not model the current systems in the convection zone or the corona, but can be used to extrapolate their respective potential fields in the conjugate domain (corona or convection zone, respectively).

sources above, below, and through the photosphere. For practical data analysis, the summation is truncated at some $\ell_{\max}$ and Eqs. (21a)-(21c) are exact only for band-limited signals.

For contrast, consider a traditional potential field extrapolation written in terms of CICCI coefficients with convergent boundary conditions, $\boldsymbol{P} \to 0$ for $r \to \infty$ (Altschuler & Newkirk 1969; Schatten et al. 1969; Hoeksema 1984; Wang & Sheeley 1992)

$$\boldsymbol{P}(\vartheta,\varphi) = \sum_{\ell=1}^{\infty} \sum_{m=-\ell}^{\ell} \left[\ell\,(\ell+1)\,(\widetilde{P}^{<}_{\ell,m} + \widetilde{P}^{>}_{\ell,m})\,\mathbf{Y}_{\ell,m}(\vartheta,\varphi) - \ell\,(\widetilde{P}^{<}_{\ell,m} + \widetilde{P}^{>}_{\ell,m})\,\boldsymbol{\Psi}_{\ell,m}(\vartheta,\varphi)\right], \tag{22}$$

where $\boldsymbol{P}$ is assumed to be solely produced by convection zone sources and thus exclusively determined by the radial component of $\boldsymbol{B}$ in the photosphere $\mathcal{S}\,(R_\odot)$ through the spectral relationship for B_r, i.e., $\widetilde{Q}_{\ell,m} = \ell\ (\ell+1)\ (\widetilde{P}^{<}_{\ell,m} + \widetilde{P}^{>}_{\ell,m})$. Comparing the potential field extrapolation with Equations (21a)-(21c), the most obvious difference is Equation (21c), the missing toroidal field component $\boldsymbol{B}_{\rm T}$ in the potential field extrapolation, Equation (22). However, the potential extrapolation also *misattributes* the part of the radial component produced by sources in the corona ($\widetilde{P}^{>}_{\ell,m}$) to sources in the convection zone as the extrapolation is required to be convergent as $r \to \infty$. A similar misattribution occurs for the components of $\boldsymbol{P}$ in the photospheric surface, i.e., $\boldsymbol{P}_{\mathcal{S}} = \hat{\boldsymbol{r}} \times (\boldsymbol{P} \times \hat{\boldsymbol{r}})$. In contrast, while CICCI is a modest generalization of the spectral potential coronal field extrapolation, it provides quantitative attribution of magnetic fields in the photosphere to current sources in the convection zone and corona.

The nonlocal VSHTs for CICCI operate directly on the components of the magnetic field. This has two important consequences. (i) The large scale topological properties of CICCI analyses should be robust to local artifacts in the vector magnetograms. Consider the scenario of corrupted magnetic field measurements in a region $\mathcal{A}$ of the photosphere bounded by the contour $\mathcal{C}$ containing a true radial current J_r. If the corrupted observations in $\mathcal{A}$ are localized away from $\mathcal{C}$ then the CICCI toroidal magnetic field $\boldsymbol{B}_{\rm T}$ will satisfy the Ampère relation for the true radial current J_r on $\mathcal{C}$ despite the corrupted observations, i.e., $\oint_{\mathcal{C}} \boldsymbol{B}\cdot d\boldsymbol{l} = \oint_{\mathcal{C}} \boldsymbol{B}_{\rm T}\cdot d\boldsymbol{l} = 4\,\pi c^{-1} \int_{\mathcal{A}} dS\, J_r$ enclosed by $\mathcal{C}$. The corrupted magnetic field measurements in the interior of $\mathcal{A}$ do not affect $\oint_{\mathcal{C}} \boldsymbol{B}_{\rm T}\cdot d\boldsymbol{l}$ because the circulation of $\boldsymbol{B}$ on $\mathcal{C}$ is unaffected by the corrupted pixels inside $\mathcal{A}$. Thus, CICCI provides a robust visual and the quantitative means to detect radial current systems without differentiating $\boldsymbol{B}$ in $\boldsymbol{x}$-space. Robust vortical features in $\boldsymbol{B}_{\rm T}$ imply the presence of a net radial current. (ii) The CICCI analysis does not require spatial differentiation of the magnetic field observations. Indeed, $Q\,(R_\odot,\vartheta,\varphi)$ is as smooth as B_r and $S\,(R_\odot,\vartheta,\varphi)$ and $T\,(R_\odot,\vartheta,\varphi)$ are substantially smoother than the tangential components of the magnetic field because $\widetilde{S}_{\ell,m} \sim \ell^{-2}$ and $\widetilde{T}_{\ell,m} \sim \ell^{-2}$. Thus, CICCI will redistribute noise amongst the components $\boldsymbol{B}^{<}_{\rm P}$, $\boldsymbol{B}^{>}_{\rm P}$, and $\boldsymbol{B}_{\rm T}$ but will not increase the noise in the reconstructed field $\boldsymbol{B}$. However, CICCI is susceptible to biases caused by substantial changes in the disambiguation of the magnetic field.

The speed and accuracy of spherical harmonic transforms have significantly improved in recent decades (McEwen & Wiaux 2011; Seljebotn 2012; Leistedt et al. 2013; Reinecke & Seljebotn 2013; Schaeffer 2013). Recently, a very fast vector spherical harmonic transform library SHTns has been developed by Schaeffer (2013) (see https://nschaeff.bitbucket.io/shtns/). These transforms are accurate to spherical harmonic degree $\ell = 16383$ (at least), which is roughly 4 times the instrumental sampling of the HMI images. CICCI has been implemented in an object-oriented library in Interactive Data Language (IDL) to call SHTns routines through a shared library of C-wrappers for analyzing data.

3. VALIDATION OF CICCI WITH MHD MODELING

MHD simulations are an essential tool for understanding solar observations, as they provide a comprehensive description of large scale plasma phenomena above the photosphere. CICCI provides indirect information about the structure of atmospheric current systems, but direct attribution of photospheric fields to coronal currents is a key step for validation and understanding the solar observations. To achieve this connection, a Cartesian version of CICCI was used to analyze an MHD simulation described in Knizhnik et al. (2017) that was performed with the Adaptively Refined MHD Solver (ARMS, Devore 1991; DeVore & Antiochos 2008).

The simulations in Knizhnik et al. (2017) implement flux preserving boundary conditions, sometimes colloquially referred to as line-tied boundary conditions (e.g., Antiochos et al. 1999; Aulanier et al. 2005; Karpen et al. 2012), on the surface between the guard cells and the interior of the ARMS simulation—this $z \equiv 0$ surface is defined as the magnetic boundary of ARMS. Boundary conditions are imposed at several different z locations within the simulation to achieve flux conservation on the magnetic boundary $z = 0$ with the staggered mesh implemented by ARMS. For the velocity, the simulation is driven at the cell centers ($z = 1/2$) which are just above the magnetic boundary. Homogenous

Neumann boundary conditions are applied to $\boldsymbol{B}_{\mathcal{S}}$ (face centered) and $\boldsymbol{v}$ (cell centered) across the cells $z = \pm 1/2$ that share a face with the magnetic boundary, i.e. $\partial \boldsymbol{B}_{\mathcal{S}}/\partial z = 0$ and $\partial \boldsymbol{v}/\partial z = 0$ at $z = 0$. These interleaved boundary conditions preserve B_z to numerical precision at the magnetic boundary $z = 0$ for boundary driven flows that are restricted to regions where B_z is a constant and $\boldsymbol{\nabla}_{\mathcal{S}} \cdot \boldsymbol{v}_{\mathcal{S}} = 0$, where $\boldsymbol{\nabla}_{\mathcal{S}} \cdot \boldsymbol{v} \equiv \boldsymbol{\nabla} \cdot \boldsymbol{v} - \partial v_z/\partial z$ in Cartesian geometry.

The normal component of the magnetic field B_z through the magnetic boundary $z = 0$ is initialized with a cylindrically symmetric sunspot in the coordinate system $r = \sqrt{x^2 + y^2}$ and $\theta = \arctan(x, y)$ where $(x, y) = (0, 0)$ corresponds to the center of the lower boundary. The sunspot is modeled by a circular positive polarity, $B_z(r) > 0$ for $r < a$, surrounded by an annulus of negative polarity, $B_z(r) < 0$ for $r > a$ where a is the radius of the PIL (see Knizhnik et al. 2017, for a complete description of the simulation's initial conditions). The magnetic field, defined by the normal component of $\boldsymbol{B}$ at $z = 0$, is initially potential $\boldsymbol{B} = \boldsymbol{P}_0$ in the simulation volume. This is driven at $z = 1/2$ by 199 small-scale rotational vortices distributed across the positive polarity $B_z > 0$ in the sunspot. The sign, $\pm$, of the vorticity for each vortex was assigned randomly, so that the net helicity injected into the sunspot is close to zero. The initial distribution of B_z is preserved exactly at the simulation magnetic boundary $z = 0$ by the driving at $z = 1/2$ in a nearly uniform region interior to the PIL. The simulation data, stored on a staggered grid, is all interpolated to the same horizonal locations in a single vertical $z = 1/2$ surface of the simulation denoted the "photosphere" below. The vertical field B_z is not perfectly preserved everywhere in this surface.

Deep into the evolution of this simulation, the fields and current systems in the MHD volume were examined and the photosphere ($z = 1/2$) was analyzed with a Cartesian version of CICCI. The results of this analysis are shown in Figure 4. The top left panel shows the *total* normal magnetic field at the photosphere in grayscale and field lines (green tubes) of the *total* magnetic field $\boldsymbol{B}$ integrated from the photosphere. The distribution of B_z in the photosphere is mostly unchanged by the vortical flows, and so B_z total remains predominantly cylindrically symmetric. Nonetheless, the green magnetic field lines in the simulation have been perturbed by the vortex driving and have gained some shear.

The right column of panels display the CICCI magnetic components $\boldsymbol{B}_{\mathrm{T}}$ and $\boldsymbol{B}_{\mathrm{P}}^{>}$ in the photosphere produced by vertical currents through this surface and currents above this surface, respectively. In both right-hand panels, the grayscale represents the normal magnetic component of the coronal sources $B_{\mathrm{P}n}^{>}$ for context and the tangential magnetic components are shown as red (cyan) vectors over positive (negative) normal magnetic field, to enhance visibility. The yellow contour represents the PIL corresponding to $B_z = \hat{\boldsymbol{n}} \cdot \left(\boldsymbol{B}_{\mathrm{P}}^{<} + \boldsymbol{B}_{\mathrm{P}}^{>}\right)$ and the blue contours correspond to the PILs of just the $B_{\mathrm{P}n}^{>}$ component. Three immediate conclusions may be drawn from the CICCI magnetograms in the right column. First, $\boldsymbol{B}_{\mathrm{T}}$ (upper right) shows regions of magnetic vorticity corresponding to vertical currents. In particular, the white arrow in the right top panel corresponds to a counterclockwise magnetic vortex and the black arrow corresponds to a clockwise vortex. The structure of the toroidal field, $\boldsymbol{B}_{\mathrm{T}}$, reveals current channels leaving (white arrow) and entering (black arrow) the "convection zone" outside the simulation through the magnetic boundary. Second, $\boldsymbol{B}_{\mathrm{P}}^{>}$ (lower right) shows numerous radially aligned PILs with the in-plane field in inverse polarity configurations that diverge from negative and converge to positive polarity, consistent with the presence of a few dozen current channels above these PILs with their axes aligned radially from the center of the sunspot. The path of one such current channel follows the PIL of $B_{\mathrm{P}n}^{>}$ from the white arrow to the black arrow, consistent with the inverse polarity of the in-plane components of $\boldsymbol{B}_{\mathrm{P}}^{>}$ along that segment of the PIL. Third, CICCI *can provide information about how the origin of B_z on a surface has changed even when the value of B_z has not changed on the surface!* For example, in this simulation the corona now contains a current system that produces $B_{\mathrm{P}n}^{>}$ in the photosphere, as indicated by the grayscale images in the right columns. Because of these evolving simulation currents, the "convection zone" outside the simulation must produce additional image currents to preserve $B_z = B_{\mathrm{P}n}^{<} + B_{\mathrm{P}n}^{>}$ on the magnetic boundary at $z = 0$ (flux-conserving conditions). Whether the sun's convection zone generates image currents in response to the evolution of coronal currents is an open question. Regardless, many coronal MHD simulations impose flux-conserving (sometimes called line tied) photospheric driving, which implies the generation of these image currents outside the simulation (Mikić & Linker 1994; Kusano et al. 1995; Amari et al. 1996; Antiochos et al. 1999; Zuccarello et al. 2015; Dahlin et al. 2019).

To provide context for these conclusions derived from the CICCI analysis, we examined the current systems in the MHD simulation volume. While the total field lines (green) shown in the upper left panel do not directly exhibit strong evidence for current channels, the absence of this evidence in the *total* magnetic field is not surprising. The current channels that we infer from CICCI, i.e., $\boldsymbol{B}_{\mathrm{T}}$ and $\boldsymbol{B}_{\mathrm{P}}^{>}$, correspond to the magnetic components produced by just the coronal currents in the simulation volume, which are superimposed upon the (much stronger) potential field above the magnetic boundary produced *mostly but not entirely* by the convection zone currents, i.e., $\boldsymbol{B}_{\mathrm{P}}^{<} \approx \boldsymbol{P}_0$. The lower

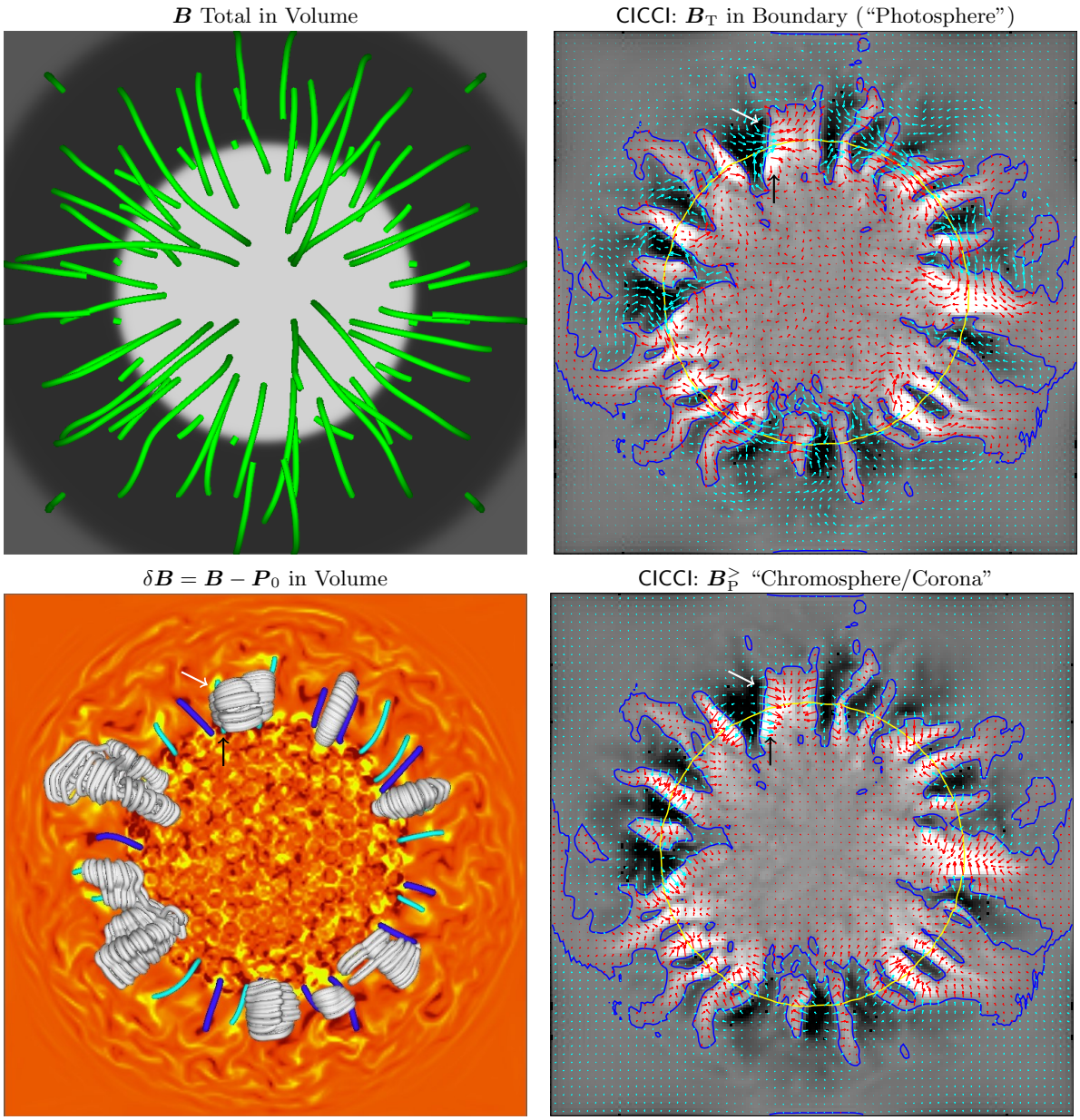

Figure 4. Analysis of fields in Knizhnik et al. (2017) MHD simulation (see text). Top left: B_z in photosphere (grayscale) plus $\boldsymbol{B}$ field lines. Top right: $\boldsymbol{B}_{\rm T}$ in photosphere superimposed on $B_{{\rm P}n}^{>}$. Bottom left: normal current in the photosphere (orange), current field lines (blue, rooted in positive J_z inside the PIL, and cyan, rooted in negative J_z inside the PIL), and $\delta\boldsymbol{B}$ magnetic field lines (gray). Bottom right: $\boldsymbol{B}_{\rm P}^{>}$ in the photosphere.

left panel brings this, and the story, home. Here, selected gray field lines are computed by subtracting the original potential field from the total field in the simulation $\delta\boldsymbol{B} = \boldsymbol{B} - \boldsymbol{P}_0$. For context, this visualization is combined with the blue (cyan) current systems originating (terminating) in the sunspot and the normal component of current at the photosphere in a white (positive)-orange-black (negative) color scale, which shows the honeycomb of vertical current sources produced by the vortices driving evolution of the sunspot's corona. The blue and cyan current systems can be seen to connect positive photospheric normal current to negative normal current, and where field lines are plotted, to lie along the core of the white twisted field lines of $\delta\boldsymbol{B}$. As inferred from CICCI analysis, there is a bare current channel, wrapped up in a twisted field line, connecting the white to the black arrows.

4. APPLICATION TO AR 12673

The mathematical analyses and application to MHD data presented above demonstrates that CICCI provides direct quantifiable attribution of vector magnetic fields to current systems above, below, and through the observed surface $\mathcal{S}\,(R_\odot)$. This suggests that the application of CICCI to ARs can reveal important relationships and even suggest coronal connections between current systems passing through the photosphere. To reveal the origin of the photospheric magnetic field, a spherical version of CICCI was developed and applied to SDO/HMI vector magnetic field observations of AR 12673. The results, presented below, are paradigm shifting. They suggest that bare or partially dressed currents are directly detectable from photospheric observations and that a significant fraction of the radial magnetic field B_r in the photosphere is produced by coronal currents.

4.1. *Preparation of the SDO/*HMI *Vector Magnetic Field Data*

The SDO/HMI telescope pipeline produces full-Sun vector magnetic field observations at 1" resolution (sampling 0.5") with a cadence of approximately 12 minutes. HMI measures Fe I $\lambda = 6173.343$ $\mathring{A}$ filtergrams at six wavelengths and four polarizations (Hoeksema et al. 2014). The calibrated filtergrams are combined to form the four Stokes vectors I, Q, U, and V at the six wavelengths, which are then processed by the Very Fast Inversion of the Stokes Vector (VFISV) algorithm (Borrero et al. 2011; Centeno et al. 2014). The VFISV algorithm inverts the Stokes vectors based on a Milne-Eddington (ME) solar atmosphere and produces 8-10 observables including the magnitude B, and azimuth ψ, and inclination γ of the magnetic field relative to line-of-sight (LoS).

When the observed spectra do not meet the underlying assumptions of the ME thermodynamic model (e.g., strong fields or extreme velocities, lack of gradients in the ME model, or asymmetries present in the Stokes profiles, see Hoeksema et al. 2014), automated ME vector field inversions such as those produced by VFISV in the SDO/HMI pipeline are known to fail. SDO/HMI ME inversions are further limited by HMI's sparse spectral sampling with 24 observations constraining 8-10 parameters. However, ME inversion failures are not unique to the SDO/HMI pipeline, and occur, as well, in the MERLIN inversions (Lites et al. 2007) for Hinode/SOT-SP spectra,[4] though perhaps with less frequency than for SDO/HMI due to the higher spatial and spectral resolution of Hinode/SOT-SP relative to SDO/HMI. Nonetheless, the SDO/HMI data represent the highest resolution temporally synchronized spatially distributed observations of the full disk photospheric vector magnetic field that are uncorrupted by the spatial distortions produced by atmospheric seeing, and thus, in our judgment, the best overall data set for the first application of CICCI. Several failure modes for SDO/HMI VFISV pipeline ME inversions have been described in Figures 13 and 14 of Hoeksema et al. (2014), and these were used as a guide to develop the objective automated detection and repair algorithm for corrupted SDO/HMI VFISV pipeline ME inversions, which is described in the Appendix A. This repair algorithm is applied to all SDO/HMI images prior to analysis with CICCI, unless otherwise explicitly stated below.

In strong field regions, the 180° ambiguity in the azimuth (Harvey 1969) is resolved with the Minimum Energy (ME0) code (Metcalf 1994; Leka et al. 2009; Hoeksema et al. 2014). For this study, the quiet sun fields are disambiguated with the angle that is most consistent with a potential field $\boldsymbol{P}$. This effectively minimizes the energy in the photospheric magnetic field produced by coronal currents, but quiet sun fields are largely ignored in the subsequent analysis. After disambiguation and repair of corrupted measurements, the vector fields in the LoS coordinate system may then be transformed into spherical vectors $\boldsymbol{B} = (B_r, B_\theta, B_\phi)$ in the photosphere $\mathcal{S}\,(R_\odot)$.

Presently, simultaneous measurements of the solar vector magnetic field are possible exclusively on the full disk, which represents only half of the Sun—leaving the farside of the Sun unobserved. The tilt between the solar rotation axis and the ecliptic plane produces an annual variation in the fraction of the poles observed by HMI. This annual variation, characterized by the *solar-b angle*, complicates the VSHT in Stonyhurst coordinates (Thompson 2006) because the data observed on the solar disk is generally discontinuous at different longitudes as a function of Stonyhurst latitude. For the purposes of this analysis, the Sun is treated as periodic and the discontinuity in observations is mitigated by remapping (interpolating) and transforming the vector magnetic field into the *spherical-$\boldsymbol{b}$* coordinate system $(B_r, B_\vartheta, B_\varphi)$ with $\vartheta = 0°$ aligned with the normal to the ecliptic plane and $(r, \vartheta, \varphi) = (R_\odot, 90°, 0°)$ corresponding to the center of the observed solar disk. After the VSHT and decomposition to $\boldsymbol{B}^{<}_{\rm P}$, $\boldsymbol{B}^{>}_{\rm P}$, and $\boldsymbol{B}_{\rm T}$ is accomplished, the resulting surface vector components, e.g., $(B^{>}_{{\rm P}\vartheta}, B^{>}_{{\rm P}\varphi})$, are *rotated* back into the traditional *spherical-$\boldsymbol{\omega}$* spherical coordinate system $(B^{>}_{{\rm P}\theta}, B^{>}_{{\rm P}\phi})$, where $\theta = 0°$ is aligned with the solar rotation axis. However, to avoid further remapping interpolations, while the vector fields are transformed to the traditional spherical-$\boldsymbol{\omega}$ spherical coordinate, the data is left on the (ϑ, φ) coordinates, but could be remapped to (θ, ϕ) or the native image pixel grid (i, j) for further analysis. There are several

[4] https://www2.hao.ucar.edu/csac/csac-data/sp-data-description

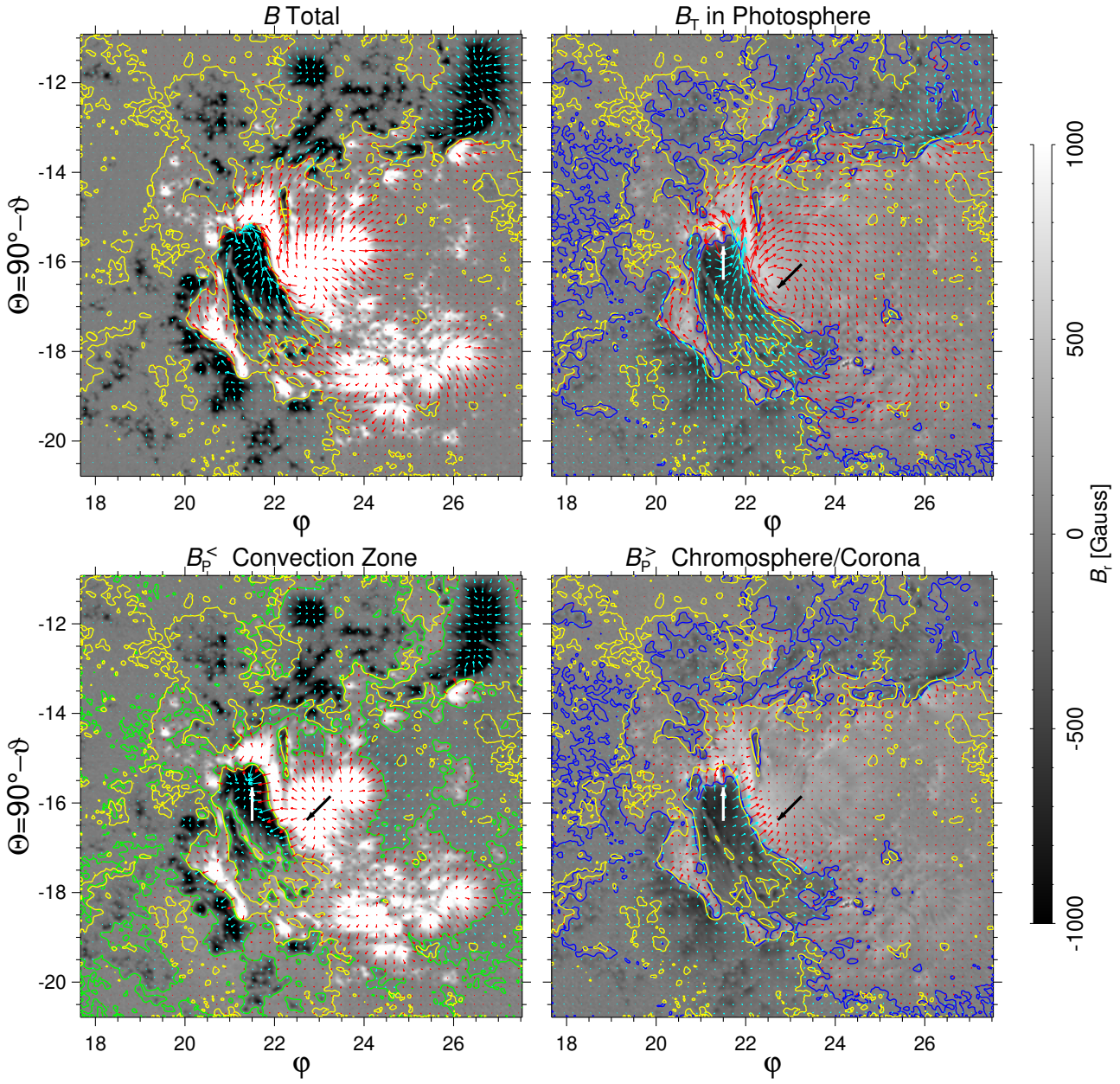

Figure 5. The vector magnetic field and the three components of the CICCI decomposition $\boldsymbol{B}_{\rm T}$, $\boldsymbol{B}_{\rm P}^{<}$, and $\boldsymbol{B}_{\rm P}^{>}$ for HMI observations of AR 12673 on 2017 September 05 at 11:58:42. The color scale in each panel, saturated at ±1000 G, represents the radial field B_r (top left panel), $B_{{\rm P}r}^{<}$ (bottom left), or $B_{{\rm P}r}^{>}$ (right panels). The contours in each panel represent the PILs of B_r (yellow), $B_{{\rm P}r}^{<}$ (green), or $B_{{\rm P}r}^{>}$ (blue). The surface magnetic field vectors originating in negative (positive) polarities are represented in cyan (red). Each of the surface vectors represents the average of 81 CICCI estimates (pixels) or ≃ 34 HMI estimates (pixels). The vectors in the right-hand panels are enhanced by a factor of 2 relative to the left-hand panels, for visualization purposes.

other non-periodic techniques to fill in the missing vector fields on the farside of the Sun and these will be investigated in future work.

4.2. *Application of CICCI to AR 12673*

CICCI was applied to SDO/HMI observations of AR 12673, which emerged with multiple pairs of dipoles east of a decaying remnant from ARs 12665 and 12670 on 29-Aug-2017 and produced 27 M-class flares and four X-class flares, including the largest flare of Solar Cycle 24, during its disk passage from 2017 August-2017 September 10 (Sun &

Norton 2017; Yang et al. 2017). For these *first light* results, the CICCI calculations were performed with $\ell = 8192$ for a sampling rate of $\Delta\varphi \simeq 180°/\ell = 0.022°$ on a Gauss grid based on Gauss-Legendre quadrature. This grid over-samples the HMI observations by approximately a factor of 1.4 at the disk center $\Delta\varphi_{\rm HMI} = 0.030°$, with increased oversampling toward the solar limb where the spatial resolution of the observational data decreases due to the projection of the LoS of each pixel onto the solar surface. The resampling factors for AR 12673, which is off disk center, are 1.7 along the abscissa and 1.4 along the ordinate relative to the raw SDO/HMI images. The SDO/HMI vector field inversions contained some corrupted measurements (inversion failures) that occur preferentially near the neutral line in AR 12673. These were automatically detected and repaired by the algorithm described in the Appendix. Figure 5 shows the CICCI vector magnetic field decomposition of AR 12673 from HMI observations on 2017 September 05 at 11:58:42, which corresponds to a quiet time, following a period that produced 10 M-class flares in 24 hr, between an M3.8 flare ending at 06:43 and an M2.3 flare beginning at 17:37, both produced by AR 12673 (see Table 1 in Yang et al. 2017). The color scale in each panel, saturated at ±1000 G, represents the radial field B_r (top left panel), $B_{{\rm P}r}^{<}$ (bottom left), or $B_{{\rm P}r}^{>}$ (right panels). The contours in each panel represent the PILs of B_r (yellow), $B_{{\rm P}r}^{<}$ (green), or $B_{{\rm P}r}^{>}$ (blue). The top left panel exhibits the total vector magnetic field $\boldsymbol{B}$ where surface magnetic field vectors originating in negative (positive) polarities are represented in cyan (red) for visualization purposes. Each of the surface vectors represents the average of 81 CICCI estimates (pixels) or $\simeq 34$ HMI estimates (pixels), i.e., between a 5×6 and 6×7 averaging and down-sampling of the original HMI resolution. The top right panel shows the toroidal component $\boldsymbol{B}_{\rm T}$ of the CICCI decomposition, which satisfies $\boldsymbol{B}_{\rm T}\cdot\hat{\boldsymbol{r}} = 0$, as surface vectors (the surface vectors in the right-hand panels are enhanced by a factor of 2 relative to the left two panels, for visualization). The toroidal component $\boldsymbol{B}_{\rm T}$ is produced by radial currents J_r passing through the photosphere and thus $\boldsymbol{B}_{\rm T}$ exhibits significant vorticity. The bottom left panel shows the CICCI component $\boldsymbol{B}_{\rm P}^{<}$ produced by convection zone currents. The green PILs, corresponding to $B_{{\rm P}r}^{<}$, differ significantly from the yellow PILs, corresponding to B_r. PILs are essentially how flux partitions are defined in the photosphere and these differences complicate estimating the current balance in the PIL by the traditional methods discussed in § 1, as bare or partially dressed coronal current systems inherently change the flux surfaces in the photosphere. The bottom right panel shows the CICCI component $\boldsymbol{B}_{\rm P}^{>}$ produced by coronal currents. The blue PILs shown here, corresponding to $B_{{\rm P}r}^{>}$, again differ significantly from the yellow PILs, corresponding to $B_r = B_{{\rm P}r}^{>} + B_{{\rm P}r}^{<}$. Note that the surface vectors diverge from negative polarities and converge at positive polarities. This signature is a familiar situation for certain observations, termed *inverse polarity* PILs (see review by Gibson 2018) or *bald patches* (Titov et al. 1993). As the source of the coronal field is presumably usually dominated by convection zone sources, such inverse polarity PILs are rare for the full $\boldsymbol{B}$, but when CICCI is used to isolate only coronal sources, they become the dominant signature in $\boldsymbol{B}_{\rm P}^{>}$. While these inverse PILs can be found both for potential (Titov et al. 1993) and non-potential coronal field (Figure 5 lower right panel), CICCI is able to definitively distinguish between a bald patch produced by the convection zone and the corona.

Figure 5 displays a clear example of CICCI's capability to reveal the photospheric signature of *current channels in the convection zone and the corona.* The lower left panel shows the field in the photosphere produced by the convection zone. The extent of the flux distributions shown here is $\sim 2° - 4°$ or 25-50 Mm which, as has been noted in other AR studies (e.g., Toriumi et al. 2014; McClintock & Norton 2016), is roughly the scale of supergranulation ~ 30 Mm (e.g., Hirzberger et al. 2008). While a unique current system cannot be determined from surface measurements alone, the photospheric vector field produced by the convection zone is consistent with a convection zone current channel directed from north to south along the PIL between the white and black arrows. Figure 6 displays a schematic diagram of this scenario. The left panel shows a side view of an idealized convection zone current system (red) below the photosphere (gold). The partially dressed convection zone current system produces a potential coronal field $\boldsymbol{P} = -\boldsymbol{\nabla}\Phi$ sheathed by return current (cyan) above the dashed arch. The right panel shows the top down view of the corresponding photospheric response in B_r. The sign of the radial flux in the right panel is represented by the black (negative) and white (positive) color scale and dashed and solid contours, respectively.

The upper right panel of Figure 5 shows a pair of vortical magnetic field patterns in $\boldsymbol{B}_{\rm T}$ indicated by the white arrow (counterclockwise vortex) and the black arrow (clockwise). These two magnetic vortex structures are robust features of AR 12673, occurring in every CICCI magnetogram that we have visually inspected (in particular 20 minutes before and after 2017 September 05 at 11:58:42) and also occurring in CICCI analysis of the raw (unrepaired) SDO/HMI pipeline inversions from 2017 September 05 at 11:58:42. Indeed, there were no substantial differences visually, or in terms of the scientific inferences, between the CICCI analyses of the raw data and data repaired by the algorithm described in the Appendix. This CICCI analysis reveals that a robust current channel is leaving the convection zone at

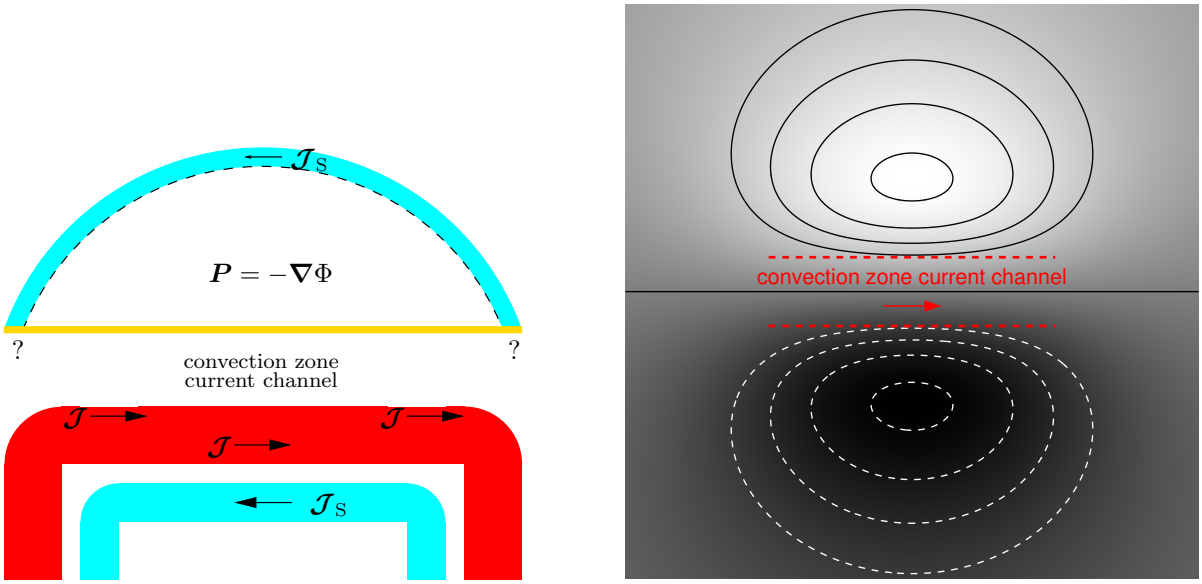

Figure 6. Schematic diagram (left) of an idealized convection zone current system and (right) corresponding photospheric response in B_r. The sign of the radial flux is represented by the black (negative) and white (positive) color scale and dashed and solid contours respectively. Question marks in the left panel indicate that the sheath current connects in some unspecified manner to the convection zone current.

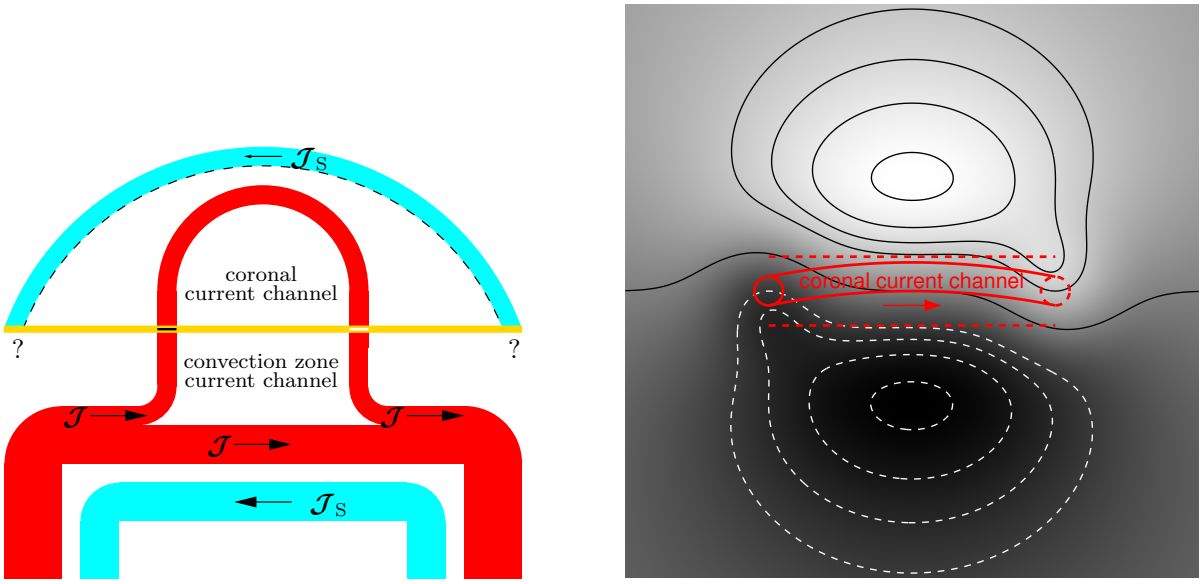

Figure 7. Schematic diagram (left) the convection zone current system and (right) corresponding photospheric response in B_r consistent with Figure 5. Here, the original convection zone current channel of Figure 6 has bifurcated to allow a channel of bare current to emerge into the corona. This emerged bare current is assumed to also carry an axial magnetic flux, represented by the black (negative) and white (positive) segments at the photosphere (gold). The coronal current channel (red arch) enters/leaves the corona at the white/black arrows in Figure 5. Question marks in the left panel indicate that the sheath current connects in some unspecified manner to the convection zone current.

the white arrow and one is entering the convection zone at the black arrow. The bottom right panel, corresponding to the photospheric field produced by coronal current systems, indicates how the upward and downward current regions are connected: $\boldsymbol{B}_{\rm P}^{>}$ crosses the PIL connecting these two vortical regions in an inverse configuration, revealing that a current channel runs southward $\approx 2^\circ$ or 24 Mm through the corona between these two regions. Thus, inspection of $\boldsymbol{B}_{\rm T}$ together with $\boldsymbol{B}_{\rm P}^{>}$ reveals a current channel arching through the corona. Figure 7 displays a schematic diagram of

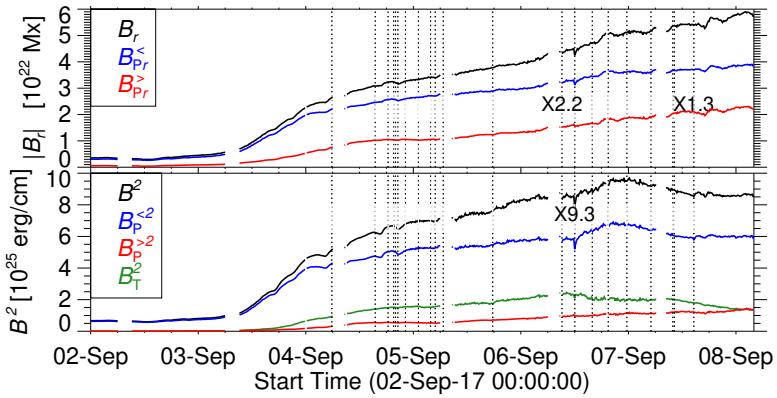

Figure 8. CICCI analysis for the evolution of AR 12673. Top: the unsigned radial flux for total field $\boldsymbol{B}$ (black) and that produced by the convection zone $\boldsymbol{B}_{\rm P}^{<}$ (blue) and the corona $\boldsymbol{B}_{\rm P}^{>}$ (red). Bottom: area integrated energy density in the photosphere for $|\boldsymbol{B}|^2$, $|\boldsymbol{B}_{\rm P}^{<}|^2$, $|\boldsymbol{B}_{\rm P}^{>}|^2$ and $|\boldsymbol{B}_{\rm T}|^2$.

the current systems that are consistent with the PIL between the black and white arrows shown in Figure 5. The left panel of Figure 7 shows a side view of a convection zone current that has bifurcated such that a portion of the current system has emerged through the photosphere and into the corona. The right panel of Figure 7 shows a top down view of the corresponding photospheric response in B_r. The convection zone current sets the large scale structure in B_r (similar to Figure 6), but this structure is modified both symmetrically by the field produced by the coronal current channel and asymmetrically by the axial flux that is assumed to be intrinsically part of the current channel, denoted by the negative (black) and positive (white) footpoints in the photosphere (gold) in the left panel of Figure 7 (note that the azimuthal currents encircling the current channel that generate this axial flux are not shown here). The combination of the convection zone current channel and the coronal current channel and its intrinsic axial magnetic flux in the photosphere produce the key photospheric signatures of Figure 5, namely (i) a bipolar AR, (ii) a *sigmoidal* S-shaped PIL (Acton et al. 1992; Rust & Kumar 1996; Canfield et al. 1999), (iii) a tangential field produced by the convection zone pointing across the PIL from positive to negative polarity, (iv) tangential field produced by the corona pointing across the PIL from negative to positive polarity and (v) the vertical current channels passing through the photosphere combine to produce a strong component of the magnetic field along the PIL.

Further inspection of upper right panel of Figure 5 reveals that the strong toroidal magnetic fields ($\boldsymbol{B}_{\rm T}$) are aligned along this PIL, suggesting the presence of a coronal arcade with strong shear field or a coronal flux rope with strong guide field paralleling both this PIL and this coronal current channel. The component of the magnetic field aligned parallel to the PIL, colloquially, if ambiguously, named the *magnetic shear*, in AR 12673 occurs because the PIL is interposed between two oppositely directed bare radial currents J_r passing through the photosphere. These bare currents provide a direct and intuitive explanation for the origin of the magnetic fields aligned along the PIL that does not require appeals to a model such as helicity condensation (Antiochos 2013) for the accumulation of magnetic shear at PILs. These insights gained from the inspection of Figure 5 demonstrate a significant benefit of the CICCI analysis: this technique can unambiguously, robustly, and quantitatively reveal important structures where they are not readily detectable from inspection of the full photospheric magnetic field.

To further demonstrate the power of CICCI analysis, consider the time evolution of AR 12673 exhibited in Fig. 8, where flares greater than M-class are denoted by the vertical dashed lines (X-class flares are labeled). The top panel shows the unsigned flux for the total magnetic field (B_r, black), and that produced by the convection zone ($B_{Pr}^{<}$, blue) and the corona ($B_{Pr}^{>}$, red). The bottom panel shows the area integrated energy density in the photosphere for the fields. For both panels the observations are integrated over the high confidence observations (determined by the segments `hmi.b720s.conf_disambig` ≥ 90 and `hmi.b720s.confid_map` < 1), i.e., low confidence (quiet sun) observations are ignored, within the area defined by the HMI Space Weather Active Region Patches (SHARPS) on the Gauss grid used by CICCI. The entire data set in Figure 8 was processed twice; once with the raw SDO/HMI Pipeline VFISV ME inversions and once where the corrupted pixels in the inversions were identified and repaired with the algorithm described in the Appendix. There was no material difference between the CICCI analysis for the two different processing strategies indicating that the scientific inferences and quantitative results derived from CICCI are robust to a few clusters of corrupted pixels.

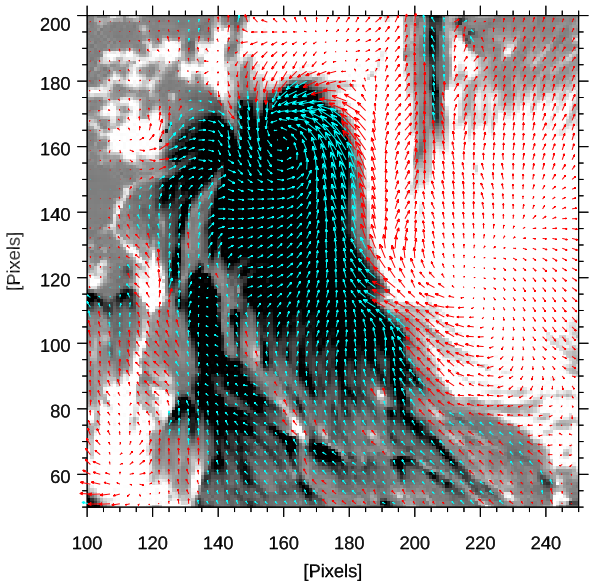

Figure 9. Hinode/SOT-SP vector magnetogram corresponding to 2017 September 05 10:51:08-11:23:28. The color scale and vectors are displayed in the same format as Figure 5.

Figure 8 exhibits new direct measures of the non-potentiality of the solar corona, all of which are rigorous mathematical and physical quantities that do not rely on any extrapolation assumptions. During the period of 2017 September 02-2017 September 03 the region consists of a potential coronal field with convection zone sources $B^{<}_{\mathrm{P}r}$ predominantly providing the radial photospheric field B_r. As new flux begins to emerge on 2017 September 03, the character of the AR becomes strongly non-potential, as indicated by the separation between B_r and $B^{<}_{\mathrm{P}r}$ and the rise of the contribution from $B^{>}_{\mathrm{P}r}$ shown in the top panel. Figure 8 shows that AR 12673 emerges and develops coronal current systems *simultaneously*, as indicated by the rise of the integrated energy density in B^2_{T} (green), which is produced by the radial current J_r, and $B^{>2}_{\mathrm{P}}$ (red) — these partially dressed current systems continue to develop long after the period of fast emergence that ends at roughly 2017 September 04 00:00. Figures 8 conclusively demonstrates that some ARs emerge concurrently with and support partially dressed current systems. Figures 5 and 8 quantitatively demonstrate that the coronal currents contribute to both the radial and tangential magnetic field in the photosphere. Note that by 2017 September 08, as shown in Figure 8, roughly 40% of the unsigned radial field B_r in the photosphere is produced by the corona, in contradiction to the prevailing paradigm that the source of the "emerged" photospheric field is the convection zone.

The evolution of AR 12673 is certainly extreme (Sun & Norton 2017). Thus, there can be legitimate concerns regarding the application of CICCI to SDO/HMI full disk data, which exhibits the failed inversions that are identified and repaired according to the algorithm described in the Appendix. To further address this, consider the AR 12673 observations by Hinode/SOT-SP (Tsuneta et al. 2008) which has higher spatial and spectral resolution in comparison to SDO/HMI. Figure 9 shows the vector magnetic field resulting from the MERLIN inversion and ME0 disambiguation of the Hinode/SOT-SP scan beginning on 2017 September 05 at 10:51:08 and ending at 11:23:28.[5] The full vector field exhibits a structure remarkably similar to the SDO/HMI magnetogram in the upper right panel of Figure 5. Note that the Hinode/SOT-SP data has not been remapped to ϑ and φ coordinates as in Figure 5. The Hinode/SOT-SP vector magnetogram displays a coherent counterclockwise magnetic vortex centered at $x = 160$ and $y = 160$ and a more subtle clockwise magnetic vortex $x = 220$ and $y = 115$. There are significant challenges to consider and overcome in applying CICCI accurately to the limited field of view, higher resolution, and rasters of non-simultaneous Hinode/SOT-SP scans and these will be developed in future publications. Nonetheless, the fact that the vector field structures directly revealed by $\boldsymbol{B}_{\mathrm{T}}$ with CICCI may be discerned in the Hinode/SOT-SP observations lends support to CICCI's application to SDO/HMI data and the robustness of the science inferences drawn from this analysis.

[5] Level 2 Hinode/SOT-SP data, doi:10.5065/D6JH3J8D

5. CONCLUSIONS

The CICCI technique combines 53 yr of spectral potential field (source surface) extrapolations in solar physics (Altschuler & Newkirk 1969; Schatten et al. 1969; Hoeksema 1984; Wang & Sheeley 1992, see also Riley et al. (2006)) with Gauß's 183 year old insight regarding the sources of the terrestrial magnetic field (Gauß 1839). This analysis when applied to the state-of-the-art solar vector magnetograms presented in this article transforms the understanding of coronal evolution. This work has conclusively presented three paradigm shifting observations revealed by CICCI analysis: (i) bare or partially dressed currents are supported by the solar corona and the fingerprints of these coronal current systems are unambiguously detectable in the photosphere using vector magnetograms, (ii) coronal current systems can be a significant source of the normal component of the magnetic field in the photosphere, and (iii) the magnetic field parallel to the PIL in AR 12673 is produced by currents through the photosphere, as reflected in $\boldsymbol{B}_{\mathrm{T}}$ which is caused solely by the radial current system J_r.

The operative question is no longer whether bare or partially dressed currents can exist in the solar atmosphere—they do—but rather whether the integrated mutual and self-Lorentz forces of these current systems play an essential role in solar eruptions by driving ideal instabilities (Chen 1989; Kliem & Török 2006). The coronal forces on an idealized direct current completely and symmetrically enclosed by a counterbalancing sheath current are substantially different when the counterbalancing sheath current is detached and spatially separated from the direct current. Indeed, these observations of bare and partially dressed current systems suggest that the *hoop force* may play a significant role in the force balance of coronal current systems (Shafranov 1966).

In addition, the robust analyses enabled by CICCI promise to bring significant new insights into our understanding of the solar atmosphere and sources of the solar wind, in particular, through CICCI's ability to distinguish between the radial photospheric magnetic field B_r generated by convection zone currents, which is therefore potential in the corona, and the photospheric B_r generated by coronal currents. The radial photospheric magnetic field and its PILs determine the coronal and heliospheric topology, namely, field line connectivity (Baum & Bratenahl 1980; Gorbachev & Somov 1988), regions of open and closed magnetic fields, which represent the respective sources of the *fast* (Zirker 1977) and *slow* solar wind (Zurbuchen 2007), the number of null points (Gorbachev et al. 1988), quasi-separatrix layers (Priest & Démoulin 1995; Demoulin et al. 1996), and ultimately structures in the heliospheric current sheet (Smith 2001; Antiochos et al. 2011). These analyses rely on the properties of the potential field (Schmidt 1964; Hagyard & Teuber 1978) or potential field source surface (PFSS) models (Altschuler & Newkirk 1969; Schatten et al. 1969) determined from the LoS field or B_r in the photosphere. As noted in Eq. (22) of § 2, the potential field misattributes coronal sources of B_r to the convection zone and thus when the corona is a significant source of radial field, as demonstrated by Figures 5 and 8, the assumption that the radial field is produced exclusively by the convection zone almost certainly leads to substantial errors in coronal topology inferred by techniques such as PFSS. With CICCI analyses, this misattribution can be unambiguously rectified.

Lastly, while the existence of potential ARs is an indisputable observational fact, the emergence and existence of these ARs inherently require the emergence of return currents and the existence of bare or partially dressed direct currents in the convection zone. Modeling the initial state of the corona as a potential field ignores the bare sheath current that is required to emerge to allow that potential field to expand into the corona and abstracts and trivializes the resulting direct current in the convection zone (see Figures 1, 2, 6, and 7).

A forthcoming paper will develop the concepts and mathematical analysis presented in this article in more detail, including the development of Monte Carlo uncertainty estimates for the components of CICCI and investigating the impact of different approaches for filling in the missing farside data.

The authors acknowledge useful conversations with Lars Daldorff, Spiro Antiochos, Judy Karpen, and Nathanaël Schaeffer. The authors acknowledge support from the NASA Internal Science Funding Model (H-ISFM) program "Magnetic Energy Buildup and Explosive Release in the Solar Atmosphere" (Schuck, Leake); the Center for HelioAnalytics (GSFC) (Schuck); the NASA Living with a Star (H-LWS) Focused Science Topic programs: NNH17ZDA001N-LWS "Developing Vector Magnetic Maps from SDO/HMI that can Drive Space Weather Models" (Schuck), NNH16ZDA001N-LWS "Implementing and Evaluating a Vector-Magnetogram-Driven Magnetohydrodynamic Model of the Magnetic Field in the Low Solar Atmosphere" (Leake, Linton, Schuck), and NNH17ZDA001N-LWS "Investigating Magnetic Flux Emergence with Modeling and Observations to Understand the Onset of Major Solar Eruptions" (Linton, Schuck, Leake); the NASA Supporting Research (H-SR) programs: NNH18ZDA001N-HSR "Investigating Magnetic Flux Rope Emergence as the Source of Flaring Activity in Delta-Spot Active Regions" (Knizhnik, Linton), and NNH17ZDA001N-HGIO "Electric-Current Neutralization in Solar Active Regions and its Relation to

Table 1. Parameters used for the objective identification of corrupted pixels

	0	1	2
χ_i^2	500	—	100
δB_i [G]	1000	150	500
τ_i	—	5	5

Magnetic Shear and Eruptive Activity" (Leake); and from the Office of Naval Research (Linton, Knizhnik). Resources supporting this work were provided by the NASA High-End Computing (HEC) Program through the NASA Center for Climate Simulation (NCCS) at Goddard Space Flight Center.

SDO data was supplied courtesy of the SDO/HMI and SDO/AIA consortia. SDO is the first mission to be launched for NASA's Living With a Star (LWS) Program. Hinode is a Japanese mission developed and launched by ISAS/JAXA, collaborating with NAOJ as a domestic partner, NASA and STFC (UK) as international partners. The scientific operation of the Hinode mission is conducted by the Hinode science team organized at ISAS/JAXA. This team mainly consists of scientists from institutes in the partner countries. Support for the post-launch operation is provided by JAXA and NAOJ(Japan), STFC (U.K.), NASA, ESA, and NSC (Norway).

APPENDIX

A. THE OBJECTIVE IDENTIFICATION AND REPAIR OF CORRUPTED PIXELS

As noted in the main text, the SDO/HMI VFISV pipeline ME inversions are known to fail occasionally. These failures sometimes manifest as individual and sometimes in clusters of corrupted pixels that exhibit values that are substantially different from the surrounding pixels. Causes and examples of these failures are discussed and presented in Figures 13-14 in Hoeksema et al. (2014). For individual vector magnetograms, visual examination of the data to identify and tag corrupted pixels for the application of a repair algorithm may be appropriate (Anfinogentov et al. 2019). However, this approach is both subjective and labor intensive when the interest is in studying the long time behavior of ARs. Presently there is not a standardized objective procedure beyond that implemented by the SDO/HMI pipeline for identifying and repairing VFISV ME inversion failures. This appendix presents the first objective method for identifying and repairing them. We expect future improvements can be made to enhance the accuracy of both the identification and repair algorithms, the two key steps in the reconstruction of the corrupted data.

A.1. *The Objective Identification of Corrupted Pixels*

The first step in repairing SDO/HMI VFISV pipeline ME inversion failures is their objective identification. The SDO/HMI `hmi.b_720s` series combines the VFISV ME inversions with the ME0 disambiguation and provides a wealth of diagnostic data. We have found the following segments the most useful for identifying bad pixels: `chisq` (χ^2 of the VFISV solution), `field_err` (uncertainty in B), `confid_map` (updated confidence index), `conv_flag` (flag and index of VFISV convergence), `conf_disambig` (confidence of the disambiguation result), and `inclination` (see Tables 3, 4, 6, and 10 in Appendix A of Hoeksema et al. 2014). Using these criteria, a nominal set of corrupted pixels is determined from

$$\text{repair}_0 = \left[\left(\texttt{chisq} > \chi_0^2\right) \vee \left(\texttt{field\_err} > \delta B_0\right) \vee \left(\texttt{confid\_map} = 5\right) \vee \left(\texttt{conv\_flag} \neq 0\right)\right] \wedge \left(\texttt{conf\_disambig} \geq 60\right), \tag{A1}$$

where the parameters are given in Table 1, $\wedge$ is the logical `AND` operator, and $\vee$ is the logical `OR` operator. This criterion tags both failures identified as part of the pipeline processing as well as extreme χ^2 values and extreme errors in the magnitude of the field B. In particular, the SDO/HMI pipeline tags bad pixels defined as aberrant compared with adjacent pixels with `confid_map` = 5. The `conf_disambig` ≥ 60 criterion restricts identification to just pixels that are annealed as part of the full disk disambiguation (eliminating, in particular, a large fraction of pixels containing

weak magnetic field and pixels off the solar disk). These pixels, identified by repair_0, are then replaced by a quick and dirty repair "$\mathtt{Mean}_4$" consisting of collecting the nearest neighbors (at least four) followed by dropping the high and low value and taking the distance weighted mean of the remaining pixels.[6]

However, as Hoeksema et al. (2014) notes in section 7.2, while some corrupted pixels are easily identified by large values of χ^2, the overall goodness of fit determined by VFISV, other corrupted pixels do not exhibit anomalously large values of χ^2. Thus, a second iterative stage is added to the objective identification step to consider the properties of the pixels surrounding a potentially corrupted pixel. Since the number of pixels in the neighborhood of this target is small, the median is used in place of the traditional mean to calculate the local statistics robustly. First the local median $\bar{B} = \mathrm{med}\,(B, \nu)$, deviation $\delta\bar{B} = B - \bar{B}$, and local median of the squared deviation $\bar{\sigma}_B^2 = \mathrm{med}\left(\delta\bar{B}^2, \nu\right)$ of the field magnitude are computed with a width of 5 pixels ($\nu = 5$) corresponding to 25 pixels surrounding the central pixel. Two other inversion failure modes are then identified:

$$\mathrm{repair}_1 = \left(\delta\bar{B}/\bar{\sigma}_B < -\tau_1\right) \wedge \left(|\mathtt{inclination} - 90^\circ| < 10^\circ\right) \wedge \left(\mathtt{field\_err} > \delta B_1\right) \wedge \left(\mathtt{conf\_disambig} \geq 60\right), \tag{A2}$$

$$\mathrm{repair}_2 = \left(\delta\bar{B}/\bar{\sigma}_B < -\tau_2\right) \wedge \left(\mathtt{field\_err} > \delta B_2\right) \wedge \left(\mathtt{chisq} > \chi^2_2\right) \wedge \left(\mathtt{conf\_disambig} \geq 60\right). \tag{A3}$$

Both failure modes consider aberrant pixels that exhibit considerably weaker field than the neighboring *uncorrupted* pixels (five standard deviations below the median value), noting that the previous stage has nominally repaired all of the previously known corrupted pixels. The first failure mode is associated with inclinations very close to 90°, i.e., magnetic fields nearly tangent to the photosphere, and is less tolerant of errors in the field than repair_0. Most of the failures in the region of interest correspond to the range $0^\circ < \mathtt{inclination} - 90^\circ < 10^\circ$. Note that, in contrast, few of the failures in this region of interest correspond to the range $-10^\circ < \mathtt{inclination} - 90^\circ < 0^\circ$. The second failure mode ignores the inclination of the field but is more tolerant of field errors than repair_1 and incorporates the χ^2. The criterion for the failure mode repair_1 is very similar in structure to repair_0, but involves exclusively the logical AND operator $\wedge$ and incorporates information about the deviation of B from the median of the surrounding pixels. The pixels identified by repair_1 and repair_2 are then also nominally repaired by the quick and dirty $\mathtt{Mean}_4$ procedure described above and this iterative stage is repeated until no more corrupted pixels are detected. Certainly these criteria can be refined in future work, particularly for corrupted data in umbra with $\mathtt{inclination} \approx 0^\circ$ or $\mathtt{inclination} \approx 180^\circ$, but we found that these failure modes detected the vast majority of the visually obvious corrupted pixels during the disk passage of AR 12673.

A.2. *The Objective Repair of Corrupted Pixels*

Once the corrupted pixels are identified, there are inevitable trade-offs to be made to accomplish the repair. Two different techniques were investigated for repairing the corrupted pixels. The first technique replaced the observations of the corrupted pixel with the average of its nearest uncorrupted neighbors using the quick and dirty approach described above using a minimum of four ($\mathtt{Mean}_4$) and eight ($\mathtt{Mean}_8$) nearest neighbor pixels (these repair algorithms are very similar to that in Anfinogentov et al. 2019). The second technique applied a radial basis function fit (RBFF) to the data to repair the corrupted pixels. Radial basis functions have been applied successfully to reconstruct missing data in natural images (see, e.g., Hardy 1971, 1990; Uhlir & Skala 2005). RBFF has significant advantages over a simple mean of the neighboring pixels: (i) RBFs have been shown to be a universal approximator and appropriate for the design of neural networks (Park & Sandberg 1991); (ii) RBFs can predict values for missing data that are both larger and smaller than the neighboring data.

The objective of the RBFF is to predict the value of a corrupted pixel at $\boldsymbol{x}_\mathrm{c}$ with a fit to a selection of N_P neighboring uncorrupted pixels with values $g = g_0, \ldots, g_{N_\mathrm{P}-1}$ at N_P scattered locations $\boldsymbol{x} = \boldsymbol{x}_0, \ldots, \boldsymbol{x}_{N_\mathrm{P}-1}$. The fit minimizes the weighted sum of the squares

$$\chi^2 = \sum_{i=0}^{N_\mathrm{P}-1} w_i \left[G\left(\boldsymbol{x}_i\right) - g_i\right]^2, \tag{A4}$$

where the function $G\left(\boldsymbol{x}\right)$ is represented by a sum of RBFs $\Phi\left(|\boldsymbol{x}|\right)$ defined as

$$G\left(\boldsymbol{x}\right) = \sum_{j=0}^{N_\mathrm{B}-1} \alpha_j \, \Phi\left(|\boldsymbol{x} - \boldsymbol{x}_j|\right), \tag{A5}$$

[6] To add statistical robustness Michael Liu's and Marshall Perrin's suggestions of tossing out the high and low values before averaging with inverse distance weighting were implemented (see https://www.stsci.edu/~mperrin/software/sources/fixpix.pro).

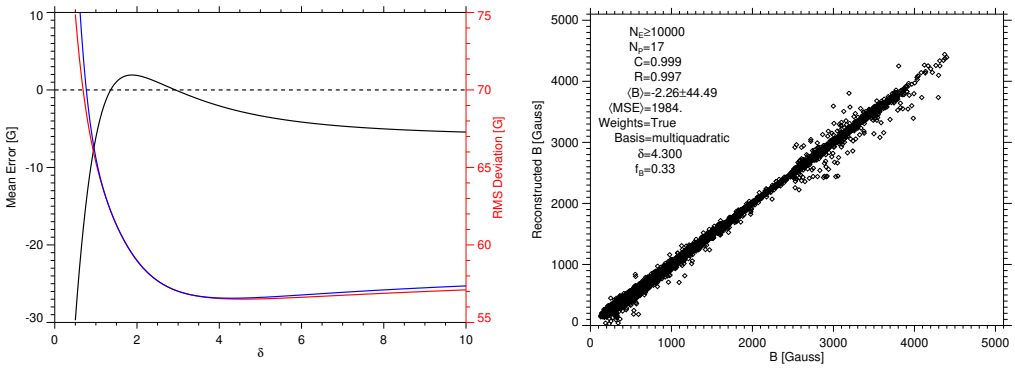

Figure 10. Calibration of RBFF (left panel): Mean error (black, left axis), standard deviation (red, right axis), and root mean squared error (blue, right axis) for $N_{\rm E} = 10,000$, $N_{\rm P} = 17$ and $f_{\rm B} = 0.33$ as a function of the scale parameter δ for B from the VFISV pipeline ME inversion at 2017 September 6 05:58:42. The minimum of the mean squared error occurs at $\delta = 4.3$. Right panel: validation of RBFF for 2017 September 05 at 23:58:42 with a scatter plot of reconstructed B vs. observed B for $N_{\rm E}$ pixels tagged as corrupted to test the RBFF. The parameters used for validation and statistical results are inset in the plot where C and R are the Pearson and Spearman rank correlation coefficients respectively.

where $N_{\rm B} \leq N_{\rm P}$ and $N_{\rm B} = N_{\rm P}$ correspond to interpolation (see, e.g., Mongillo 2011). Once the coefficients α_j are determined by minimizing Equation (A4), the function $G(\boldsymbol{x})$ may be used to forecast the corrupted value $G(\boldsymbol{x}_{\rm c})$.

There are a variety of choices for the RBFs $\Phi(|\boldsymbol{x}|)$. In this study, the Hardy function, also called the multiquadric RBF (Hardy 1971), was implemented,

$$\Phi(r) = \sqrt{r^2 + \delta^2}, \tag{A6}$$

with inverse distance weighting $w_i = |\boldsymbol{x}_{\rm c} - \boldsymbol{x}_i|^{-2}$. Alternatively, the experimental uncertainties Δg_i of g_i could be used to weight the data. The parameter δ in Equation (A6) is a scale parameter that is chosen objectively from the performance of the RBFF on the data (see, e.g., Mongillo 2011).

A.3. *Calibration and Validation*

The RBFF repair algorithm is calibrated by choosing the number of $N_{\rm P}$ pixels, number of $N_{\rm B}$ radial basis functions, and δ scale parameter that performed the best for the SDO/HMI VFISV ME inversions (`hmi.b_720` series) for 2017 September 06 at 05:58:42. The calibrated parameters are then applied to data from 2017 September 05 at 23:58:42 for validation. These different, later times from 2017 September 05 at 11:58:42 in Figure 5 were chosen for calibration and validation to ensure that the repair parameters were not tuned to the time where the major scientific inferences are being drawn. In particular, the data from 2017 September 06 at 05:58:42 exhibit more corrupted pixels than from 2017 September 05 at 11:58:42 because the evolution of AR 12673 becomes more extreme as the observation time approaches the X-class flare on 2017 September 06 at 08:57.

A.3.1. *Construction of the Calibration and Validation Distributions*

Distinct ensembles of $N_{\rm E} = 10,000$ pixels from the VFISV pipeline ME inversion that were classified as uncorrupted by the identification criteria of Appendix A.1 were selected for calibration at 2017 September 06 05:58:42 and validation at 2017 September 05 at 23:58:42. Since there are vastly more observations below than above 2,500 G, all uncorrupted observations above 2,500 G were used in calibration and validation to provide some rudimentary data balancing, and the remainder of the ensembles were randomly chosen uncorrupted pixels. These ensembles were further randomized to eliminate any correlations in field strength. These ensembles of 10,000 uncorrupted pixels were then divided into batches of 500 pixels that were then all temporarily tagged as *corrupted* and repaired to provide ground truth calibration and validation statistics for the RBFF repair algorithm described in Appendix A.2.

A.3.2. *Calibration*

Accurate reconstruction is important not just for the repair of corrupted pixels but also for situations where the detection algorithm may inappropriately tag a truly uncorrupted pixel as corrupted. While optimal reconstruction performance is an important consideration, a competing desirable property is stability of the RBFF. There should not be large changes in the statistical properties of reconstructed data for small changes in the optimized parameters

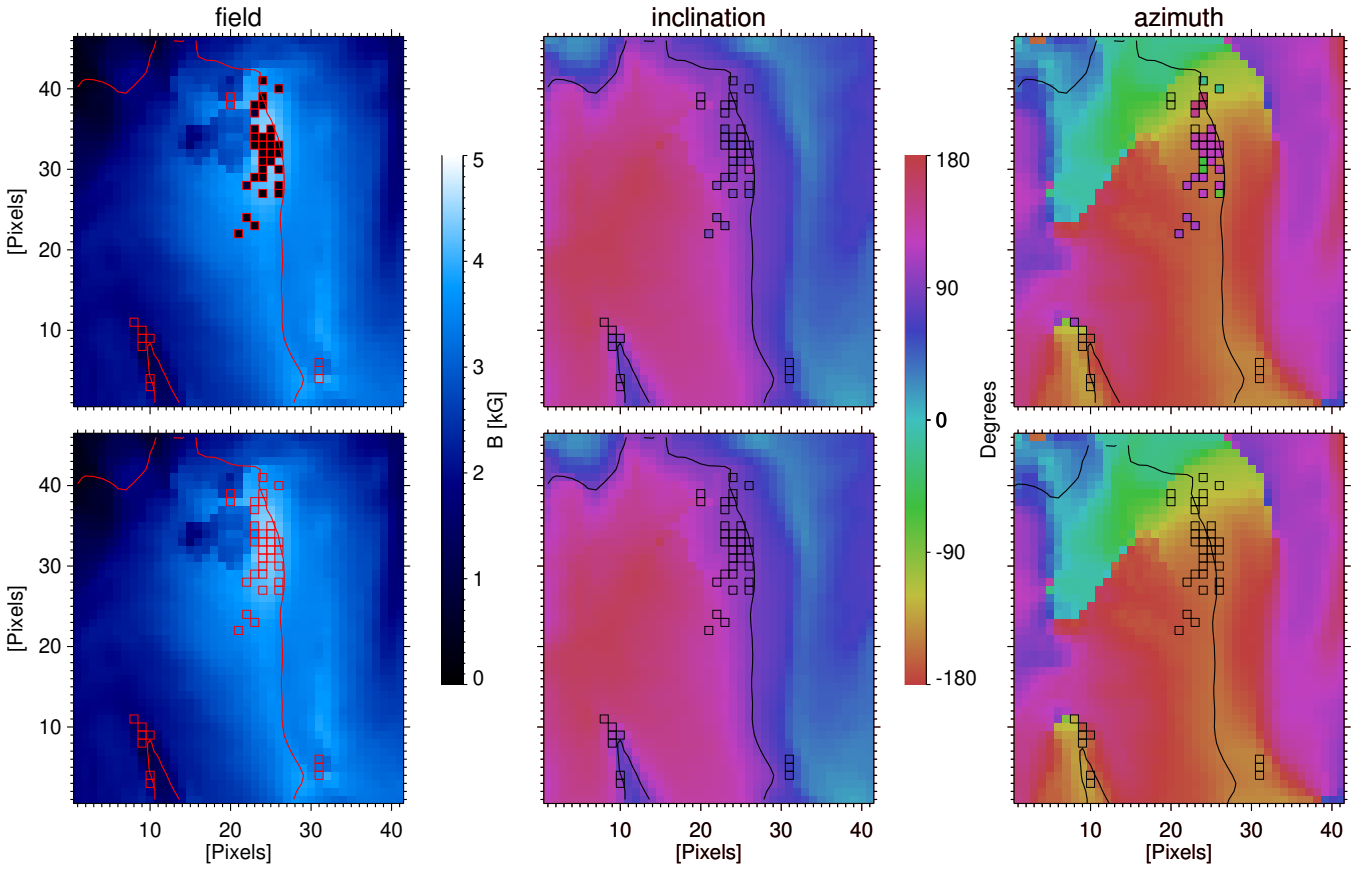

Figure 11. SDO/HMI pipeline data (top row) and the corresponding repaired data (bottom row) for the `field`, `inclination`, and `azimuth` segments of the VFISV ME inversions at 2017 September 05 at 23:58:42. The detected and repaired corrupted pixels are outlined with red or black depending on the color scale.

(Mongillo 2011). Robust reconstruction was exhibited for $N_{\rm P} \geq 17$, $N_{\rm B} \gtrsim f_{\rm B}\, N_{\rm P} \approx 6$ with $f_{\rm B} = 0.33$, which corresponds to a highly overdetermined (more data to fit than basis functions) linear least-squares fit to estimate the α_j's. Figure 10 displays the performance of the RBFF for the VFISV pipeline ME inversion at 2017 September 06 05:58:42 for the $N_{\rm E}$=10,000 pixels in the ensemble with $N_{\rm P} = 17$ and $f_{\rm B} = 0.33$. The left panel shows the mean error or bias of the repair in black, the standard deviation in red, and the root mean squared error in blue (combining bias and standard deviation). The optimal value of the scale parameter with $N_{\rm P} = 17$ and $N_{\rm B} = f_{\rm B}\, N_{\rm P} \approx 6$ with $f_{\rm B} = 0.33$ corresponds to $\delta = 4.3$, but good performance can be achieved for $\delta \approx 2 - 6$.

A.3.3. *Validation*

To validate the RBFF, the optimized repair algorithm with $N_{\rm P} = 17$, $N_{\rm B} \gtrsim f_{\rm B}\, N_{\rm P} = 6$, and $\delta = 4.3$ was applied to the validation ensemble of 10,000 pixels constructed in the same manner as described in § A.3.1 for the VFISV pipeline ME inversion at 2017 September 05 at 23:58:42. The right panel of Figure 10 shows a scatter plot of the predicted values of B versus the ground truth values in the ensemble. Overall, despite some scatter, the RBFF provides a tight correlation with the ground truth and remains largely unbiased at large values of B. The magnetic field in the basis of the CCD array (Sun 2013)

$$B_\xi = -\, B\, \sin\gamma\, \sin\psi, \tag{A7a}$$

$$B_\eta = B\, \sin\gamma\, \cos\psi, \tag{A7b}$$

$$B_\zeta = B\, \cos\gamma, \tag{A7c}$$

was constructed from the repaired pixels, where γ is the `inclination` and ψ is the disambiguated `azimuth`. The RBFF was compared to the mean square error using the quick and dirty approach of replacing the corrupted pixel with a

Table 2. Validation of RBFF: A comparison of the root mean squared error for the three repair algorithms $\texttt{Mean}_4$, $\texttt{Mean}_8$, and RBFF for the magnetic field B and the CCD basis components (B_ξ, B_η, B_ζ) corresponding to the VFISV pipeline ME inversion at 2017 September 05 at 23:58:42.

	$\sqrt{\langle \text{MSE} \rangle}$ [G]			
Repair	B	B_ξ	B_η	B_ζ
$\texttt{Mean}_4$	56.37	81.77	60.43	49.79
$\texttt{Mean}_8$	70.54	80.71	62.32	58.36
RadBF	44.51	74.40	55.17	37.52

local mean as described above with $N_\text{P} = 4$ and $N_\text{P} = 8$, denoted $\texttt{Mean}_4$ and $\texttt{Mean}_8$, respectively. Table 2 displays the performance of the three approaches on B and the components (B_ξ, B_η, B_ζ). The RBFF consistently outperforms mean squared error of the quick and dirty approaches $\texttt{Mean}_4$ and $\texttt{Mean}_8$.

Lastly, Figure 11 displays the SDO/HMI pipeline data (top row) and the repaired data (bottom row) for the `field`, `inclination`, and `azimuth` segments. The corrupted pixels detected are outlined with red or black depending on the color scale. The detection algorithm detects all the obvious aberrant pixels in the field magnitude and a few other clusters. As an example of these other clusters, consider the three pixels at located at the abscissa=31 that do not stand out as aberrant in the field magnitude. The `conv_flag` segment for these pixels is set to two indicating that the "maximum number of iterations [was] reached without converging", i.e., failure to converge for the ME inversion of these pixels by VFISV (see Table 6 in Hoeksema et al. 2014). Thus, according to the criteria outlined in Appendix A.1 these pixels have been correctly detected and identified as corrupted. Visually, the repaired data overall appears consistent with the larger scale spatial distribution of magnetic field, inclination, and azimuth.

The RBFF with $N_\text{P} = 17$, $N_\text{B} = 1/3\, N_\text{P} \approx 6$, $\delta = 4.3$ was applied to all SDO/HMI data in this paper prior to CICCI analysis except where explicitly stated. The scientific inferences drawn from the SDO/HMI data were identical with and without the repair step, suggesting that CICCI analysis is robust to local artifacts in the data. Indeed, a comparison of the downsampled vector fields of the CICCI analysis in Figure 3 and time-series in Figure 8 using corrupted and repaired data were visually indistinguishable.

REFERENCES

Acton, L., Tsuneta, S., Ogawara, Y., et al. 1992, Science, 258, 618, doi: 10.1126/science.258.5082.618

Altschuler, M. D., & Newkirk, G. 1969, SoPh, 9, 131, doi: 10.1007/BF00145734

Amari, T., Luciani, J. F., Aly, J. J., & Tagger, M. 1996, ApJL, 466, L39, doi: 10.1086/310158

Anfinogentov, S. A., Stupishin, A. G., Mysh'yakov, I. I., & Fleishman, G. D. 2019, The Astrophysical Journal, 880, L29, doi: 10.3847/2041-8213/ab3042

Antiochos, S. K. 2013, ApJ, 772, 72, doi: 10.1088/0004-637X/772/1/72

Antiochos, S. K., DeVore, C. R., & Klimchuk, J. A. 1999, ApJ, 510, 485, doi: 10.1086/306563

Antiochos, S. K., Mikić, Z., Titov, V. S., Lionello, R., & Linker, J. A. 2011, ApJ, 731, 112, doi: 10.1088/0004-637x/731/2/112

Aulanier, G., Démoulin, P., & Grappin, R. 2005, A&A, 430, 1067, doi: 10.1051/0004-6361:20041519

Aulanier, G., Török, T., Démoulin, P., & DeLuca, E. E. 2010, ApJ, 708, 314, doi: 10.1088/0004-637X/708/1/314

Backus, G. 1986, Reviews of Geophysics, 24, 75, doi: 10.1029/RG024i001p00075

Barrera, R. G., Estevez, G. A., & Giraldo, J. 1985, European Journal of Physics, 6, 287, doi: 10.1088/0143-0807/6/4/014

Baum, P. J., & Bratenahl, A. 1980, SoPh, 67, 245, doi: 10.1007/BF00149805

Biot, J.-B., & Savart, F. 1820, Ann. Chem. Phys, 15, 222. https://e-magnetica.pl/ref/biot-savart_1820
Borrero, J. M., Tomczyk, S., Kubo, M., et al. 2011, SoPh, 273, 267, doi: 10.1007/s11207-010-9515-6
Canfield, R. C., Hudson, H. S., & McKenzie, D. E. 1999, Geophysical Research Letters, 26, 627, doi: https://doi.org/10.1029/1999GL900105
Centeno, R., Schou, J., Hayashi, K., et al. 2014, SoPh, 289, 3531, doi: 10.1007/s11207-014-0497-7
Chandrasekhar, S. 1961, Hydrodynamic and hydromagnetic stability, International series of monographs on physics (New York: Oxford, Clarendon Press)
Chen, J. 1989, ApJ, 338, 453, doi: 10.1086/167211
Cheung, M. C. M., & Isobe, H. 2014, Living Reviews in Solar Physics, 11, 3, doi: 10.12942/lrsp-2014-3
Cheung, M. C. M., Schüssler, M., Tarbell, T. D., & Title, A. M. 2008, ApJ, 687, 1373, doi: 10.1086/591245
Dahlin, J. T., Antiochos, S. K., & DeVore, C. R. 2019, ApJ, 879, 96, doi: 10.3847/1538-4357/ab262a
Dalmasse, K., Aulanier, G., Démoulin, P., et al. 2015, ApJ, 810, 17, doi: 10.1088/0004-637X/810/1/17
Demoulin, P., Henoux, J. C., Priest, E. R., & Mandrini, C. H. 1996, A&A, 308, 643
Devore, C. R. 1991, Journal of Computational Physics, 92, 142
DeVore, C. R., & Antiochos, S. K. 2008, ApJ, 680, 740, doi: 10.1086/588011
Fan, Y. 2001, ApJL, 554, L111, doi: 10.1086/320935
—. 2009, Living Reviews in Solar Physics, 6, 4, doi: 10.12942/lrsp-2009-4
Fan, Y., & Liu, T. 2019, Frontiers in Astronomy and Space Sciences, 6, 27, doi: 10.3389/fspas.2019.00027
Fursyak, Y. A., Kutsenko, A. S., & Abramenko, V. I. 2020, SoPh, 295, 19, doi: 10.1007/s11207-020-1584-6
Gauß, C. F. 1839, Resultate aus den Beobachtungen des magnetischen Vereins im Jahre 1838, ed. C. F. Gauss & W. Weber (Leipzig: Weidmannsche Buchhandlun), 1–57
Georgoulis, M. K., Titov, V. S., & Mikić, Z. 2012, ApJ, 761, 61, doi: 10.1088/0004-637X/761/1/61
Gibson, S. E. 2018, Living Reviews in Solar Physics, 15, 7, doi: 10.1007/s41116-018-0016-2
Glassmeier, K.-H., & Tsurutani, B. T. 2014, History of Geo- and Space Sciences, 5, 11, doi: 10.5194/hgss-5-11-2014
Gorbachev, V. S., Kelner, S. R., Somov, B. V., & Shvarts, A. S. 1988, Soviet Ast., 32, 308
Gorbachev, V. S., & Somov, B. V. 1988, SoPh, 117, 77, doi: 10.1007/BF00148574
Gosain, S., Démoulin, P., & López Fuentes, M. 2014, ApJ, 793, 15, doi: 10.1088/0004-637X/793/1/15
Hagenaar, H. J. 2001, ApJ, 555, 448, doi: 10.1086/321448
Hagyard, M. J., & Teuber, D. 1978, SoPh, 57, 267, doi: 10.1007/BF00160101
Hardy, R. L. 1971, Journal of Geophysical Research (1896-1977), 76, 1905, doi: https://doi.org/10.1029/JB076i008p01905
—. 1990, Computers Math. Applic., 19, 163
Harvey, J. W. 1969, PhD thesis, National Solar Observatory
Hirzberger, J., Gizon, L., Solanki, S. K., & Duvall, T. L. 2008, SoPh, 251, 417, doi: 10.1007/s11207-008-9206-8
Hoeksema, J. T. 1984, PhD thesis, Stanford University, California
Hoeksema, J. T., Liu, Y., Hayashi, K., et al. 2014, SoPh, 289, 3483, doi: 10.1007/s11207-014-0516-8
Karpen, J. T., Antiochos, S. K., & DeVore, C. R. 2012, The Astrophysical Journal, 760, 81. http://stacks.iop.org/0004-637X/760/i=1/a=81
Kliem, B., & Török, T. 2006, PhRvL, 96, 255002, doi: 10.1103/PhysRevLett.96.255002
Klimchuk, J. A., & Sturrock, P. A. 1992, ApJ, 385, 344, doi: 10.1086/170943
Knizhnik, K. J., Antiochos, S. K., DeVore, C. R., & Wyper, P. F. 2017, ApJL, 851, L17, doi: 10.3847/2041-8213/aa9e0a
Kontogiannis, I., Georgoulis, M. K., Park, S.-H., & Guerra, J. A. 2017, SoPh, 292, 159, doi: 10.1007/s11207-017-1185-1
Kurokawa, H. 1991, in Flare Physics in Solar Activity Maximum 22, ed. Y. Uchida, R. C. Canfield, T. Watanabe, & E. Hiei, Vol. 387 (Berlin, Heidelberg: Springer Berlin Heidelberg), 39–50, doi: 10.1007/BFb0032613
Kusano, K., Suzuki, Y., & Nishikawa, K. 1995, ApJ, 441, 942, doi: 10.1086/175413
Leistedt, B., McEwen, J. D., Vandergheynst, P., & Wiaux, Y. 2013, A&A, 558, A128, doi: 10.1051/0004-6361/201220729
Leka, K. D., Barnes, G., & Crouch, A. 2009, in Astronomical Society of the Pacific Conference Series, Vol. 415, The Second Hinode Science Meeting: Beyond Discovery-Toward Understanding, ed. B. Lites, M. Cheung, T. Magara, J. Mariska, & K. Reeves, 365–+
Leka, K. D., Canfield, R. C., McClymont, A. N., & van Driel-Gesztelyi, L. 1996, ApJ, 462, 547, doi: 10.1086/177171
Lites, B., Casini, R., Garcia, J., & Socas-Navarro, H. 2007, Mem. Soc. Astron. Italiana, 78, 148
Liu, Y., Sun, X., Török, T., Titov, V. S., & Leake, J. E. 2017, The Astrophysical Journal, 846, L6, doi: 10.3847/2041-8213/aa861e

MacTaggart, D. 2011, A&A, 531, A108, doi: 10.1051/0004-6361/201117099
McClintock, B. H., & Norton, A. A. 2016, ApJ, 818, 7, doi: 10.3847/0004-637X/818/1/7
McClymont, A. N., & Fisher, G. H. 1989, Washington DC American Geophysical Union Geophysical Monograph Series, 54, 219, doi: 10.1029/GM054p0219
McEwen, J. D., & Wiaux, Y. 2011, IEEE Transactions on Signal Processing, 59, 5876, doi: 10.1109/TSP.2011.2166394
Melrose, D. B. 1991, ApJ, 381, 306, doi: 10.1086/170652
—. 1995, ApJ, 451, 391, doi: 10.1086/176228
—. 1996, The Astrophysical Journal, 471, 497, doi: 10.1086/177985
—. 2017, Journal of Geophysical Research: Space Physics, 122, 7963, doi: https://doi.org/10.1002/2017JA024035
Metcalf, T. R. 1994, SoPh, 155, 235, doi: 10.1007/BF00680593
Mikić, Z., & Linker, J. A. 1994, ApJ, 430, 898, doi: 10.1086/174460
Mongillo, M. A. 2011, in Society for Industrial and Applied Mathematics Undergraduate Research Online, Vol. 4 (University City, Philadelphia: Society for Industrial and Applied Mathematics), 190, doi: 10.1137/11S010840
Morse, P. M., & Feshbach, H. 1953, International Series in Pure and Applied Physics, Vol. 2, Methods in Theoretical Physics (New York: McGraw-Hill Pubublishing Co.)
Norton, A. A., Jones, E. H., Linton, M. G., & Leake, J. E. 2017, ApJ, 842, 3, doi: 10.3847/1538-4357/aa7052
Otsuji, K., Kitai, R., Ichimoto, K., & Shibata, K. 2011, PASJ, 63, 1047, doi: 10.1093/pasj/63.5.1047
Park, J., & Sandberg, I. W. 1991, Neural Computation, 3, 246
Parker, E. N. 1984, ApJ, 283, 343, doi: 10.1086/162312
—. 1996a, ApJ, 471, 485, doi: 10.1086/177983
—. 1996b, ApJ, 471, 489, doi: 10.1086/177984
Piddington, J. H. 1978, Ap&SS, 55, 401, doi: 10.1007/BF00642267
Priest, E. R., & Démoulin, P. 1995, J. Geophys. Res., 100, 23443, doi: 10.1029/95JA02740
Reinecke, M., & Seljebotn, D. S. 2013, A&A, 554, A112, doi: 10.1051/0004-6361/201321494
Riley, P., Linker, J. A., Mikić, Z., et al. 2006, ApJ, 653, 1510, doi: 10.1086/508565
Rust, D. M., & Kumar, A. 1996, ApJL, 464, L199+
Schaeffer, N. 2013, Geochemistry, Geophysics, Geosystems, 14, 751, doi: 10.1002/ggge.20071
Schatten, K. H., Wilcox, J. M., & Ness, N. F. 1969, SoPh, 6, 442, doi: 10.1007/BF00146478
Schmidt, H. U. 1964, NASA Special Publication, 50, 107
Schrijver, C. J., & Zwaan, C. 2000, Solar and Stellar Magnetic Activity, Cambridge astrophysics series (New York: Cambridge University Press)
Seljebotn, D. S. 2012, ApJS, 199, 5, doi: 10.1088/0067-0049/199/1/5
Shafranov, V. D. 1966, Reviews of Plasma Physics, 2, 103
Smith, E. J. 2001, J. Geophys. Res., 106, 15819, doi: 10.1029/2000JA000120
Sun, X. 2013, On the Coordinate System of Space-Weather HMI Active Region Patches (SHARPs): A Technical Note. https://arxiv.org/abs/1309.2392
Sun, X., & Norton, A. A. 2017, Research Notes of the American Astronomical Society, 1, 24, doi: 10.3847/2515-5172/aa9be9
Tanaka, K. 1991, SoPh, 136, 133, doi: 10.1007/BF00151700
Thompson, W. T. 2006, A&A, 449, 791, doi: 10.1051/0004-6361:20054262
Titov, V. S., Priest, E. R., & Demoulin, P. 1993, A&A, 276, 564
Toriumi, S., Hayashi, K., & Yokoyama, T. 2014, ApJ, 794, 19, doi: 10.1088/0004-637X/794/1/19
Török, T., Leake, J. E., Titov, V. S., et al. 2014, ApJL, 782, L10, doi: 10.1088/2041-8205/782/1/L10
Tsuneta, S., Ichimoto, K., Katsukawa, Y., et al. 2008, SoPh, 249, 167, doi: 10.1007/s11207-008-9174-z
Uhlir, K., & Skala, V. 2005, in 2005 13th European Signal Processing Conference, IEEE (Antalya, Turkey: IEEE), 1–4. https://ieeexplore.ieee.org/document/7078048
Vishniac, E. T. 1995, ApJ, 451, 816, doi: 10.1086/176268
Wang, Y. M., & Sheeley, N. R., J. 1992, ApJ, 392, 310, doi: 10.1086/171430
Wheatland, M. S. 2000, ApJ, 532, 616, doi: 10.1086/308577
Yang, S., Zhang, J., Zhu, X., & Song, Q. 2017, ApJL, 849, L21, doi: 10.3847/2041-8213/aa9476
Zirker, J. B. 1977, Reviews of Geophysics, 15, 257, doi: https://doi.org/10.1029/RG015i003p00257
Zuccarello, F. P., Aulanier, G., & Gilchrist, S. A. 2015, ApJ, 814, 126, doi: 10.1088/0004-637X/814/2/126
Zurbuchen, T. H. 2007, Annual Review of Astronomy and Astrophysics, 45, 297, doi: 10.1146/annurev.astro.45.010807.154030
Zwaan, C. 1978, SoPh, 60, 213, doi: 10.1007/BF00156523
—. 1985, SoPh, 100, 397, doi: 10.1007/BF00158438